THE ASTROPHYSICAL JOURNAL, 495:346–369, 1998 March 1

A RADIATION HYDRODYNAMIC MODEL FOR PROTOSTELLAR COLLAPSE. I. THE FIRST COLLAPSE

HIROHIKO MASUNAGA,[1] SHOKEN M. MIYAMA, AND SHU-ICHIRO INUTSUKA
Division of Theoretical Astrophysics, National Astronomical Observatory, Mitaka, Tokyo 181, Japan; masunaga@milano.mtk.nao.ac.jp, miyama@yso.mtk.nao.ac.jp, inutsuka@yso.mtk.nao.ac.jp
Received 1997 July 14; accepted 1997 October 10

ABSTRACT

Dynamical collapse of a molecular cloud core and the formation of a star are investigated by performing radiation hydrodynamic calculations in spherical symmetry. The angle-dependent and frequency-dependent radiative transfer equation is solved without any diffusion approximations, and the evolution of the spectral energy distribution (SED) is examined.

In the present paper, as the first step in a series of our work, evolutions before hydrogen molecules begin to dissociate (the so-called first collapse) are examined for different masses and initial temperatures of the parent cloud cores and for different opacities. Numerical results for a typical case [$T_{\rm init} = 10$ K and $\kappa_P(10\ {\rm K}) \sim 0.01\ {\rm cm^2\ g^{-1}}$] show that the radius and mass of the first core are ~ 5 AU and $\sim 0.05\ M_\odot$, respectively. These values are *independent* both of the mass of the parent cloud core and of the initial density profile. The analytical expressions for the radius, mass, and accretion luminosity of the first core are also obtained. The SED contains only cold components of a few times 10 K throughout the first collapse phase, because the opaque envelope veils the first core from observers. We suggest that the molecular cloud cores with luminosities higher than $\sim 0.1\ L_\odot$ should contain young protostars deep in the center, even if they show no evidence for the existence of central stars in near-infrared and optical observations.

Subject headings: hydrodynamics — ISM: clouds — methods: numerical — radiative transfer — stars: formation

1. INTRODUCTION

Protostellar evolution has been investigated actively during the past two decades. A standard evolutionary scenario for the formation of isolated low-mass stars can be briefly summarized as follows (e.g., Larson 1969).

The scenario begins with the gravitational collapse of a molecular cloud core. The collapse is initiated by the ambipolar diffusion of magnetic fields that supported the cloud core against gravitational collapse (e.g., Shu, Adams, & Lizano 1987; Shu 1995).

The collapsing cloud core is initially optically thin to the thermal emission from dust grains, and the compressional heating rate by the collapse is much smaller than the cooling rate by the thermal radiation. The cloud therefore collapses isothermally.

The isothermal condition is broken when the optical depth of the entire cloud core becomes of the order of unity, or when the compressional heating rate overwhelms the radiative cooling rate. The collapsing cloud thus forms an adiabatic core at its center, which is the so-called "first core." The evolution at this phase is called the "first collapse."

When the central temperature reaches about 2000 K, hydrogen molecules begin to dissociate into atoms. Because released gravitational energy is consumed by the dissociation, gas pressure cannot increase rapidly enough to support the first core against its self-gravity, and then the "second collapse" begins. After the dissociation is completed, the "second core" is born.

The surrounding envelope continues to infall through the "main accretion phase." The gas cloud with significant angular momentum forms a protoplanetary disk around the central star. The infalling gas is thermalized by the shock at the surface of the star or the disk. The thermal radiation from the shocked region is absorbed and reemitted by the envelope. Therefore, an observer can only see infrared emission from the outer envelope until material in the envelope becomes sufficiently transparent to the radiation from the central objects. Bipolar outflows are supposed to be associated with this phase of evolution.

When the accreting envelope becomes transparent to optical light, the star and protoplanetary disk appear as a T Tauri star. The dynamical evolution of a protostar is followed by the quasi-static contraction of the central star and the hypothetical viscous evolution of the protoplanetary disk.

Theoretical investigations of the above scenario involve accurate solutions of two-dimensional or three-dimensional radiation magnetohydrodynamic equations, which inevitably require numerical calculations. At present, however, the computational facilities do not have sufficient power for this task, and therefore a number of simplifications are supposed in such investigations. In the past studies that dealt with the radiative energy transport, the diffusion (or Eddington) approximations and/or the gray approximation are often introduced for simplicity. For instance, both were assumed by Larson (1969) and Appenzeller & Tscharnuter (1974). In recent works, Boss & Myhill (1992) introduced the gray three-dimensional Eddington approximation (Boss 1984) for incorporating the radiative energy transport into their radiation hydrodynamic code. The diffusion or Eddington approximation, however, is justified only in optically thick regions such as stellar interiors. Considering this point, Narita, Nakano, & Hayashi (1970) adopted the diffusion scheme only for the inner opaque region and solved the angle-dependent radiative transfer in the tenuous and extended envelope. Besides the classical diffusion approximation, the flux-limited diffusion (FLD) approximation is introduced by some recent works (Yorke, Bodenheimer, &

[1] Also at the Department of Astronomy, University of Tokyo.

Laughlin 1993, 1995). The FLD scheme saves the radiative diffusion equation from yielding unphysical solutions in optically thin regions, but still it is not assured to give the correct solutions.

The exact treatment of the radiation fields in radiation hydrodynamics (RHD) might require some simplifications on the dynamics in order to reduce the computational effort. Indeed, the past works that dealt with the radiation fields can be classified into two kinds of categories, i.e., (1) two-dimensional radiative transfer without hydrodynamics, or (2) one-dimensional RHD. The former includes Efstathiou & Rowan-Robinson (1990, 1991) and Chick, Pollack, & Cassen (1996). They calculated the temperature distributions that are consistent with the radiation fields in axisymmetry. In their calculations they fixed the density distributions as snapshots of the dynamical evolution, instead of solving the hydrodynamic equations. Moreover, the density distributions assumed by them were solutions of *isothermal* collapse, and therefore the temperature and density distributions are not self-consistent in their results.

The latter gives the self-consistent solutions with respect to all the radiation hydrodynamic quantities. A couple of comprehensive works that belong to this category were published in the same year: Stahler, Shu, & Taam (1980) and Winkler & Newman (1980a, 1980b; hereafter WNa and WNb). Stahler et al. (1980) assumed steady state inflow in the envelope and divided the problem into several parts that were solved individually, and the solutions in each part were connected at the interfaces. In contrast, WNa and WNb pursued the dynamical evolution by solving the radiation hydrodynamic equations straightforwardly using the variable Eddington factor method, which is employed also in this paper. Both of them yielded consistent results with each other, but cases other than a 1 $M_\odot$ cloud with a single initial condition were left to be examined for future investigators. Furthermore, both of them introduced the gray approximation, in which they replaced the energy mean and flux mean opacities with the Rosseland mean opacity instead of solving the frequency-dependent radiative transfer equation. The gray approximation is valid where the temperature varies spatially in a scale much larger than a mean free path of thermal photons. This is, however, not the case at the latter stage of the protostellar evolution (i.e., in the main accretion phase). Indeed, Preibisch, Sonnhalter, & Yorke (1995) showed that the gray approximation can cause considerable errors in estimating the temperature distribution and the radiative acceleration where an optically thin envelope is heated up by the central hot star.

Frequency-dependent calculations for radiation, without the gray approximation, were performed by Yorke (1979, 1980) for massive star formation. He solved the hydrodynamic equations simultaneously to see the structural evolution of a circumstellar envelope; he did not resolve the structure of the central star, but put a central radiative source there instead.

Our aim in the present investigation is to construct theoretical models that are based on the exact treatment of radiation fields by solving the angle-dependent and frequency-dependent transfer equation. Using the results of calculations, we discuss (1) conditions that change the isothermal phase into the adiabatic, (2) the radius and accretion luminosity of the first core, and (3) possible interpretations of observations. Masses and temperatures of initial molecular cloud cores are given as model parameters, in contrast to Stahler et al. (1980) and WNa and WNb. The dust opacity is also a model parameter because its dependence on frequency is uncertain. This is because of the lack of knowledge of the chemical composition, size distribution, and geometrical configuration of dust grains. We adopt spherical symmetry, which inevitably requires that the effects of rotation and magnetic fields should be neglected. Both the effects, of course, actually have important roles in protostellar evolution. Nevertheless, the spherically symmetric calculation still has significance for the following two reasons: (1) the exact treatment of radiation field in general geometry is quite difficult, and (2) moving coordinates are available only for one-dimensional calculations. A molecular cloud core of $\rho \sim 10^{-19}$ g cm^{-3} and $R \sim 0.1$ pc contracts to a star of $\bar{\rho} \sim 1$ g cm^{-3} and $R \sim 1\ R_\odot$, while the density increases by 20 orders of magnitude and the radius decreases by 6 orders. Any multidimensional numerical calculations to date that include adapted mesh refinement technique and smoothed particle hydrodynamics have not succeeded in covering such a wide dynamic range in a self-consistent way.

In the present paper, as the first step toward our final aim, we discuss the properties of the first collapse, which corresponds to the evolution prior to the dissociation of hydrogen molecules. After discussing possible contributions to observational studies in the following section, the formulation of the basic equations is presented in § 3. The initial and boundary conditions and other comments on calculations are given in § 4. The result for a typical case is overviewed in § 5. In § 6 we discuss the dependence of the radius of the first core $R_{\rm fc}$ on model parameters such as the mass, initial temperature, and opacity. We derive analytical expressions for $R_{\rm fc}$ and the accretion luminosity $L_{\rm acc}$ in § 7. We also discuss possible interpretations of observational data with our results. In § 8 we summarize the results. The computational scheme is described in Appendices A, B, and C with some useful test problems. The subsequent evolutions triggered by the second collapse will be discussed in our next paper. The formation of intermediate-mass stars ($M > 3\ M_\odot$) is also discussed in the subsequent papers.

2. POSSIBLE CONTRIBUTIONS TO OBSERVATIONS

Our frequency-dependent RHD calculations provide the emergent spectral energy distribution (SED), which has, in principle, information on the internal structure of the object. The well-known classification of the young stellar objects (YSOs)—class I, II, and III—is based on the shapes of SEDs in the near-infrared and is supposed to represent the evolutionary sequence of YSOs (e.g., see Lada 1987). The SED of class I, which is the youngest among the three, can be explained in terms of absorption and reemission (and scattering) of thermal radiation from the central objects (i.e., the star and protoplanetary disk) by the circumstellar envelope (Kenyon, Calvet, & Hartmann 1993). The definition of classes I–III requires that the objects should be seen in near-infrared light, which excludes much younger objects from the classification.

On the other hand, recent observations have discovered star-forming cloud cores without any optical or infrared sources (i.e., without *IRAS* sources). Some of them have evidence of protostellar activity such as bipolar outflows (e.g., VLA 1623 observed by André, Ward-Thompson, & Barsony 1993). André et al. (1993) considered VLA 1623 as an object younger than class I and classified it into "class

0." So-called starless cores and class 0 objects have SEDs that can be fitted with graybody spectra of T approximately a few times 10 K. These cold SEDs seem to indicate that they are substantially younger than class I protostars. Moreover, some of the starless cores are interpreted by some authors as the cloud cores contracting quasi-statically by the ambipolar diffusion of magnetic fields (Mizuno et al. 1994; Ward-Thompson et al. 1994). However, a protostar surrounded by a dense envelope might look as if it were starless even after the central stellar core was born.

The recent progress in observations demands theoretical works that model the early stage of protostellar evolution. For example, Boss & Yorke (1995) investigated early protostellar evolution and discussed the possibility that very young protostars are detected in the present and future observational projects. Our investigation, starting with the present paper, tries to model the SEDs of such very young protostellar candidates. Our suggestions about the observations will be presented briefly in § 7.4.

3. THE BASIC EQUATIONS OF RADIATION HYDRODYNAMICS

The basic equations of radiation hydrodynamics are introduced in this section. Hydrodynamic equations that account for the interactions with radiation are as follows.

$$\frac{D\rho}{Dt} + \rho\nabla\cdot\boldsymbol{v} = 0 , \tag{1}$$

$$\rho\frac{D\boldsymbol{v}}{Dt} = -\rho\nabla\Phi - \nabla p + \frac{\chi_{F0}}{c}\boldsymbol{F}_0 , \tag{2}$$

$$\rho\frac{De}{Dt} + p\nabla\cdot\boldsymbol{v} = \rho\epsilon_{\rm CR} + (c\chi_{E0}E_0 - 4\pi\chi_{P0}B) , \tag{3}$$

$$\nabla^2\Phi = 4\pi G\rho , \tag{4}$$

$$(\gamma-1)\rho e = p \equiv p(\rho, T) , \tag{5}$$

where ρ, $\boldsymbol{v}$, e, and T are the fluid mass density, the velocity, the internal energy density per unit mass, and the temperature, respectively, and χ, $\epsilon_{\rm CR}$, and γ are the absorption coefficient, the cosmic ray heating rate per unit mass, and the ratio of specific heats, respectively. The Planck function is denoted by $B \equiv \sigma T^4/\pi$. E_0 and $\boldsymbol{F}_0$, where subscript zero denotes comoving variables, are the frequency-integrated radiation energy density and radiation flux, which are defined as

$$E_0 = \int_0^\infty dv_0 \oint d\boldsymbol{\Omega}_0 I_0(v_0, \boldsymbol{n}_0) ,$$

$$\boldsymbol{F}_0 = \int_0^\infty dv_0 \oint d\boldsymbol{\Omega}_0 I_0(v_0, \boldsymbol{n}_0)\boldsymbol{n}_0 ,$$

where $I_0(v_0, \boldsymbol{n}_0)$ denotes the specific intensity of radiation at frequency v_0 along the direction vector $\boldsymbol{n}_0$ in the comoving frame. The frequency-averaged absorption coefficients are defined as follows.

$$\chi_{F0} = \frac{\int_0^\infty \chi_0(v_0)\boldsymbol{F}_0(v_0)\,dv_0}{\boldsymbol{F}_0} ,$$

$$\chi_{E0} = \frac{\int_0^\infty \chi_0(v_0)E_0(v_0)\,dv_0}{E_0} ,$$

$$\chi_{P0} = \frac{\int_0^\infty \chi_0(v_0)B(v_0)\,dv_0}{B} .$$

Equations (1)–(5) correspond to the equation of continuity, the equation of motion, the first law of thermodynamics for material, Poisson's equation, and the equation of state, respectively. They are the ordinary hydrodynamic equations except for the last terms on the right-hand side of equations (2) and (3), which describe interactions between material and radiation. To account for the radiation field exactly, the transfer equation of radiation (eq. [6]) must be solved.

$$\frac{1}{c}\frac{\partial I(v, \boldsymbol{r}, \boldsymbol{n})}{\partial t} + \boldsymbol{n}\cdot\nabla I(v, \boldsymbol{r}, \boldsymbol{n}) = -\chi(v, \boldsymbol{r})[I(v, \boldsymbol{r}, \boldsymbol{n}) - S(v, \boldsymbol{r})] , \tag{6}$$

where $S(v, \boldsymbol{r})$ is the source function. Note that equation (6) is written in the lab frame.

Because the specific intensity of radiation depends on frequency and on direction angle as well as on location, it requires considerable computational effort to solve equation (6) directly. Moreover, equation (6) must be transformed into the comoving frame to couple with the hydrodynamic equations, which would modify the equation into a quite complicated form. In contrast, it reduces the computational effort to an acceptable level to solve the moment equations of radiation in the comoving frame (eqs. [7] and [8]) instead of the transfer equation itself. The moment equations of radiation in the comoving frame were originally derived by Castor (1972) and Buchler (1979) and their studies were succeeded by Mihalas & Mihalas (1984, hereafter MM) in a comprehensive work and by Stone, Mihalas, & Norman (1992, hereafter SMN) as a two-dimensional numerical RHD code (the final work of the "ZEUS-2D" trilogy). The formulation we adopt is taken after MM and SMN, who dropped the terms that are $O(v/c)$ in all physical regimes. Therefore the adopted equations can account for all the dynamical effects of radiation in a nonrelativistic fluid (see SMN).

$$\frac{\rho}{c^2}\frac{D}{Dt}\left(\frac{\boldsymbol{F}_0}{\rho}\right) + \nabla\cdot\boldsymbol{P}_0 = -\frac{\chi_{F0}\boldsymbol{F}_0}{c} , \tag{7}$$

$$\rho\frac{D}{Dt}\left(\frac{E_0}{\rho}\right) + \nabla\boldsymbol{v}:\boldsymbol{P}_0 + \nabla\cdot\boldsymbol{F}_0 = -(c\chi_{E0}E_0 - 4\pi\chi_{P0}B) , \tag{8}$$

where $\boldsymbol{P}_0$ is the radiation stress tensor:

$$\boldsymbol{P}_0 = \int_0^\infty dv_0 \oint d\boldsymbol{\Omega} I_0(v_0, \boldsymbol{n}_0)\boldsymbol{n}_0\boldsymbol{n}_0 .$$

Equations (7) and (8) correspond to the momentum equation and the energy equation of radiation, respectively.

In our scheme, equation (3) has been replaced with the following one.

$$\rho\frac{D}{Dt}\left(e + \frac{E_0}{\rho}\right) + \nabla\boldsymbol{v}:\boldsymbol{P}_0 + \nabla\cdot\boldsymbol{F}_0 + p\nabla\cdot\boldsymbol{v} = \rho\epsilon_{\rm CR} , \tag{9}$$

which is given by taking the sum of equations (3) and (8). Equation (9) ensures that the numerical scheme will be more accurate than equation (3) when the fluid is near radiative equilibrium, because the interaction terms between material and radiation have canceled (SMN).

Equations (7) and (8) are not closed in themselves since they have been integrated over direction angle. Therefore, a closure relation that compensates the lack of knowledge for the angular distributions of the specific intensity must be given. As a closure relation, we introduce *the tensor variable Eddington factor* $\boldsymbol{f}$, which is defined by

$$\boldsymbol{P} = \boldsymbol{f} E \, . \tag{10}$$

The radiation stress tensor $\boldsymbol{P}$ is eliminated using the tensor variable Eddington factor, which is a measure of the degree of anisotropy of the radiation field, to close the system of the RHD equations.

When we calculate $\boldsymbol{f}$, the radiation field at each time step is assumed as a static snapshot under the instantaneous density and temperature distributions. In other words, we solve equation (6), neglecting the term including the time derivative. This assumption is justified only when the timescale of radiative diffusion or propagation is sufficiently short compared to the evolutionary timescale of interest. Fortunately, such a condition is satisfied in many astrophysical problems, including protostellar collapse. Even if the condition is not satisfied, the static transfer equation is still applicable for most cases in astrophysics, because the solutions from the transfer equation contribute only to the Eddington factors, which should vary less than the individual values of E and $\boldsymbol{F}$(MM). We also note that the terms of $O(v/c)$, which would appear when transforming equation (6) into the comoving frame, have been dropped because the relativistic effects such as aberration or Doppler shift hardly affect the Eddington factors for the problems of our present interest. Thus, the transfer equation is reduced to a fairly simple form and then no longer bothers us for the unacceptable computational effort.

Once $I(\nu, \boldsymbol{r}, \boldsymbol{n})$ is obtained, the monochromatic tensor variable Eddington factor is calculated using the relation:

$$\boldsymbol{f}(\nu, \boldsymbol{r}) = \frac{\boldsymbol{P}(\nu, \boldsymbol{r})}{E(\nu, \boldsymbol{r})} \, .$$

The frequency-integrated Eddington factor is defined by

$$\boldsymbol{f} = \frac{\int_0^\infty \boldsymbol{f}(\nu) E(\nu) d\nu}{E} \, .$$

The computational method, which is called the variable Eddington factor method, was established as a technique for astrophysical radiation hydrodynamics first by Tscharnuter & Winkler (1979). There is no essential difference between the computational scheme of Tscharnuter & Winkler (1979) and ours, except that they supposed the gray approximation while we solve the frequency-dependent radiative transfer equation. This method can be divided into two parts. In the first part, the transfer equation (6) with $\partial/\partial t \equiv 0$ is solved under the density and temperature distributions assumed to be known. Thus this part is called the *transfer equation solver*. The tensor variable Eddington factor at each spatial point is obtained from the solutions $I(\nu, \boldsymbol{r}, \boldsymbol{n})$. In the second part, the full set of the RHD equations (1)–(4), (7), and (9) is solved using the given Eddington factors. This part is called the *moment equations solver*. The newly obtained density and temperature distributions provide improved Eddington factors for the first part, which is employed again. The two parts are iterated in this manner for consistency. In Appendix A we will show the details of each part for the spherical symmetrical case. Test calculations are presented in Appendix B.

4. CALCULATIONS

4.1. *Initial Conditions*

For the total mass of the cloud core M_{cc}, we chose $M_{cc} = 1\ M_\odot$, $0.1\ M_\odot$, $0.3\ M_\odot$, and $3\ M_\odot$. The initial density and the radius are adjusted so that the cloud core should be slightly more massive than the Jeans mass for each case. As shown in Table 1, the initial density is $\rho_{init} \sim 10^{-20}$ to 10^{-17} g cm^{-3} (i.e., $n_{H_2} \sim 10^4$–10^7 cm^{-3}) and the radius is $R_{cc} \sim$ 1000–30,000 AU, which is compatible with the typical scales of observed molecular cloud cores. The initial density distribution is assumed to be homogeneous except for a case in which the cloud core is initially in hydrostatic equilibrium (see § 6.2). In every model, the velocity of each fluid element is set to zero in the initial state.

The initial temperature is also an important model parameter, $T_{init} = 10$, 5, and 30 K. Different initial temperatures account for possible variations of the environments in molecular clouds. Dependence of protostellar evolution on initial temperature will be discussed in § 6.3.

4.2. *Boundary Conditions*

The inner and outer boundaries are given by the center and the edge of the cloud core, respectively. The outer boundary is fixed through evolution at $R = R_{cc}$ shown in

TABLE 1

MODEL PARAMETERS

Model	M_{cc}[a] ($M_\odot$)	T_{init} (K)	$\kappa_P(T_{init})$ (cm^2 g^{-1})	ρ_{init} (g cm^{-3})	R_{cc}[b] (AU)	R_{fc}[c] (AU)	ρ_{ad}[d] (g cm^{-3})	L[e] ($L_\odot$)	L_{fc}^{acc}[f] ($L_\odot$)
M1a.....	1.0	10	1.6×10^{-2}	1.41×10^{-19}	1.0×10^4	4.2	2×10^{-13}	0.061	0.04
M2a.....	0.1	10	1.6×10^{-2}	1.41×10^{-17}	1.0×10^3	4.2	2×10^{-13}	0.014	0.04
M3a.....	0.3	10	1.6×10^{-2}	1.57×10^{-18}	3.0×10^3	4.2	2×10^{-13}	0.031	0.04
M4a.....	3.0	10	1.6×10^{-2}	1.57×10^{-20}	3.0×10^4	4.2	2×10^{-13}	0.12	0.04
C1a	1.0	5	3.2×10^{-3}	1.77×10^{-20}	2.0×10^4	3.7	1×10^{-13}	0.018	0.01
H1a	1.0	30	2.1×10^{-1}	3.82×10^{-18}	3.3×10^3	5.1	6×10^{-13}	0.24	0.3
M1b.....	1.0	10	7.7×10^{-2}	1.41×10^{-19}	1.0×10^4	6.7	5×10^{-14}	0.14	0.1
M1c.....	1.0	10	1.6×10^{-3}	1.41×10^{-19}	1.0×10^4	3.1	5×10^{-13}	0.050	0.02

[a] Mass of the parent cloud core.
[b] Radius of the parent cloud core.
[c] Radius of the first core.
[d] Estimated from the numerical results.
[e] At $\rho_c = 10^{-9}$ g cm^{-3}.
[f] Evaluated from eq. (28), with 10 for α.

Table 1. Boundary conditions for radiation involve a brief discussion as follows.

Boundary conditions for the transfer equations (A1) and (A2) (see Appendix A) are given by h_ν on the p-axis shown in Figure 13 and at the cloud edge. On the p-axis $h_\nu = 0$ because of symmetry, and h_ν at the cloud edge is determined by given incident radiation $I^-(r = R_{cc})$. In the present paper two different boundary conditions for radiation that provide a couple of extreme cases are considered.

Case 1.—There is no incident radiation but there is a heat source ϵ_{CR} to compensate for the radiative energy loss in the initial state. The heat source represents the heating by cosmic rays and photons from surrounding stars, which support the temperature of the molecular cloud against cooling by the thermal emission of dust grains (Goldsmith & Langer 1978).

Case 2.—The cloud core is surrounded by isotropic blackbody radiation of $T = T_{init}$.

Although case 2 seems to keep the cloud core naturally at a constant initial temperature, ambient blackbody radiation of T_{init} is too idealized a condition for actual molecular cloud cores. Furthermore, case 1 is more favorable than case 2 for the purpose of calculating emergent SEDs, because in case 2 incident radiation modifies the emergent spectra. In particular, in the initial state for case 2 the net flux equals zero and emergent SEDs cannot be calculated. Therefore we adopt case 1 for all the models except where indicated.

Boundary conditions of radiation moment equations (eqs. [A12] and [A13]) are given as radiation fluxes at the inner and the outer boundaries. The inner flux at the center is set equal to zero because of symmetry. The outer boundary condition differs between the two cases. In case 1, the outer flux F_{I+1} in equation (A12) is eliminated using h, where h is defined by $F_{I+1} = hcE_{I+1}$ and is given by the transfer equation solver. In case 2, the outer boundary condition for radiation is given simply by $E_{I+3/2} \equiv aT_{init}^4$, where $a \equiv 4\sigma/c$.

4.3. *Opacity*

We assume that the opacity is due to the absorption by dust grains, neglecting the scattering in this paper, and that the gas temperature couples closely with the dust temperature. These assumptions are known to be well justified in molecular cloud cores and in very young protostars. (Scattering by dust grains should be taken into account to determine the temperature structure of envelopes for more evolved young stellar objects like class I and early class II.) We have referred to Adams & Shu (1986) for frequency dependence of the dust opacity in higher frequency than far-infrared except for the line features, which have been removed in our models for simplicity. Dust grains are assumed to consist of silicate and graphite, where H_2O ice is excluded since it has no significant influences on the dynamical evolutions. The opacity for lower frequency is characterized with a parameter β, where $\kappa_\nu = \kappa_0(\nu/\nu_0)^\beta$, taking the ambiguity of the dust opacity into account. Three different models are considered with respect to β.

a) $\beta = 2.5$ for $4.6 \times 10^{11} < \nu < 3 \times 10^{12}$ Hz and $\beta = 1.5$ for $\nu < 4.6 \times 10^{11}$ Hz, taking a recent result into account (Pollack et al. 1994). [This model has a comparable value for κ_P(10 K) to that of the model of $\beta = 2$.]

b) $\beta = 1.5$ for $\nu > 3 \times 10^{12}$ Hz.

c) $\kappa_\nu = 0.1\kappa_\nu^{\text{model } a}$.

In models *a* and *b*, κ_0 is determined to be connected at $\nu_0 = 3 \times 10^{12}$ Hz with the opacity of Adams & Shu (1986), that is, $\kappa_{3\times10^{12}\,\text{Hz}} = 0.3\ \text{cm}^2\ \text{g}^{-1}$. Note that the absorption coefficients χ_ν are given with the mass opacity of dust κ_ν by $\chi_\nu(r) = \kappa_\nu \rho(r)$. We shall examine in § 6.4 how the difference among models *a*–*c* affects the evolution.

We consider the vaporization of dust grains at $T_{vap} \equiv 1200$ K. Although the molecular opacities should take the place of the opacity for higher temperature, we simply reduce the dust opacity to nearly (but not exactly) zero for $T > T_{vap}$. In order to assure the convergence of the Eddington factor between the transfer equation solver and the moment equations solver, the dust grains are supposed to vanish completely at $T = T_{vap} + \Delta T$, where ΔT is taken to be 100 K, and to decrease linearly with increase of temperature for $T_{vap} < T < T_{vap} + \Delta T$.

4.4. *Equation of State*

We adopted the equation of state of ideal gas for simplicity:

$$e = \frac{1}{\gamma - 1}\frac{k}{\mu m_H} T\ , \tag{11}$$

where γ, k, μ, and m_H are the ratio of specific heats, the Boltzmann constant, the mean molecular weight, and the mass of hydrogen atom, respectively. In the present paper, γ is fixed at 5/3 except in a case where γ equals 7/5 instead, and μ is assumed to be constant at 2.46, which corresponds to the same chemical abundance as in Larson (1969). More realistic models should include the effects of rotational and vibrational degrees of freedom for H_2 molecules, and of dissociation and ionization of the molecules. The former modifies γ from 5/3 and the latter changes the value of μ as a function of the temperature. Moreover, the dissociation and ionization energies should be taken into account in the energy equation. All of these effects will be considered in the subsequent papers.

5. RESULTS

5.1. *Overview for a Typical Case*

Results of the typical case (i.e., model M1a in Table 1) are overviewed in this section. In model M1a, the mass and the initial temperature are taken to be 1 $M_\odot$ and 10 K, respectively, with the opacity of model *a* in § 4.3. First, we present a brief summary of the results in Figures 1 and 2 with Table 2.

The initial state is indicated by the thick line in each panel. At early stages, the cloud core collapses isothermally, which corresponds to the first two lines in each panel. The

TABLE 2

ELAPSED TIMES ASSIGNED TO FIGURES 1–3

Time (10^5 yr)	Time/t_{ff} [a]	Line Type [b]
0.0	0.0	Thick
2.04830.....	1.15643	...
2.16677.....	1.22331	Dotted
2.17139.....	1.22593	...
2.17301.....	1.22684	...
2.18122.....	1.23147	Dashed
2.18725.....	1.23488	...

[a] The free-fall time is $t_{ff} \equiv [3\pi/(32G\rho_{init})]^{1/2} = 1.77 \times 10^5$ yr.

[b] For correspondence to Figs. 1 and 3.

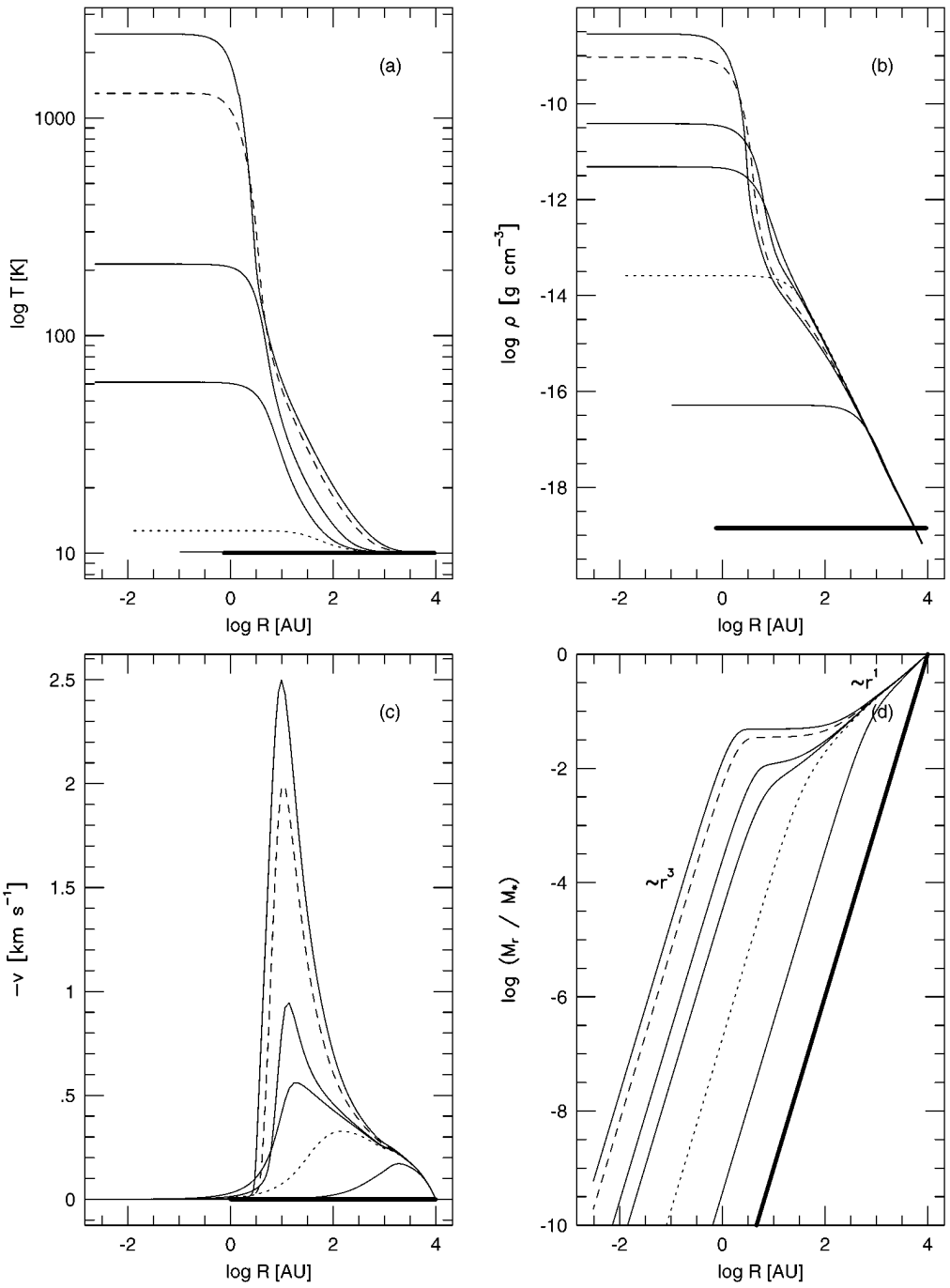

FIG. 1.—Evolutionary sequences for a typical case (model M1a) as functions of radius. Different lines in each panel represent the different elapsed times tabulated in Table 2. The initial state is specified by thick solid lines. See text for the meanings of dotted and dashed lines. The figure depicts (*a*) temperature, (*b*) density, (*c*) infall velocity, (*d*) mass, (*e*) radiation temperature, (*f*) radiative flux, (*g*) Planck mean optical depth, and (*h*) rate of change of the specific entropy.

density distribution at large radii develops an r^{-2} law reminiscent of the isothermal self-similar solution by Larson (1969) and Penston (1969; Larson-Penston solution). This isothermal stage lasts about one free-fall time until the central temperature departs significantly from the initial value (*dotted lines*). The rapid increase of the central temperature to $T \sim 2000$ K forms a central adiabatic core—that is, the first core. The drop in the density distribution at a few AU shows the effective radius of the first core, whose position gradually moves inward through the first collapse stage. The supersonically infalling gas in the envelope is decelerated and thermalized at the surface of the first core, where the shock front is observed as a sharp peak in the velocity distribution. In the radiative flux distribution, a few lines just below the dashed line have small humps at the radius of the first core, which indicates that the thermal energy generated by the shock heating is immediately radiated away. The distribution of change rate of the specific entropy shows the negative peak on the surface of the first core, where the entropy is taken out by radiation. In terms of the mass distribution, the inner region has a r^3 slope that corresponds to the homogeneous density structure inside the first core, while the outer region is proportional to the radius, which resembles the Larson-Penston solution in the infalling envelope (i.e., $\rho \propto r^{-2}$). Therefore, the plateau between these two slopes implies the mass of the first core,

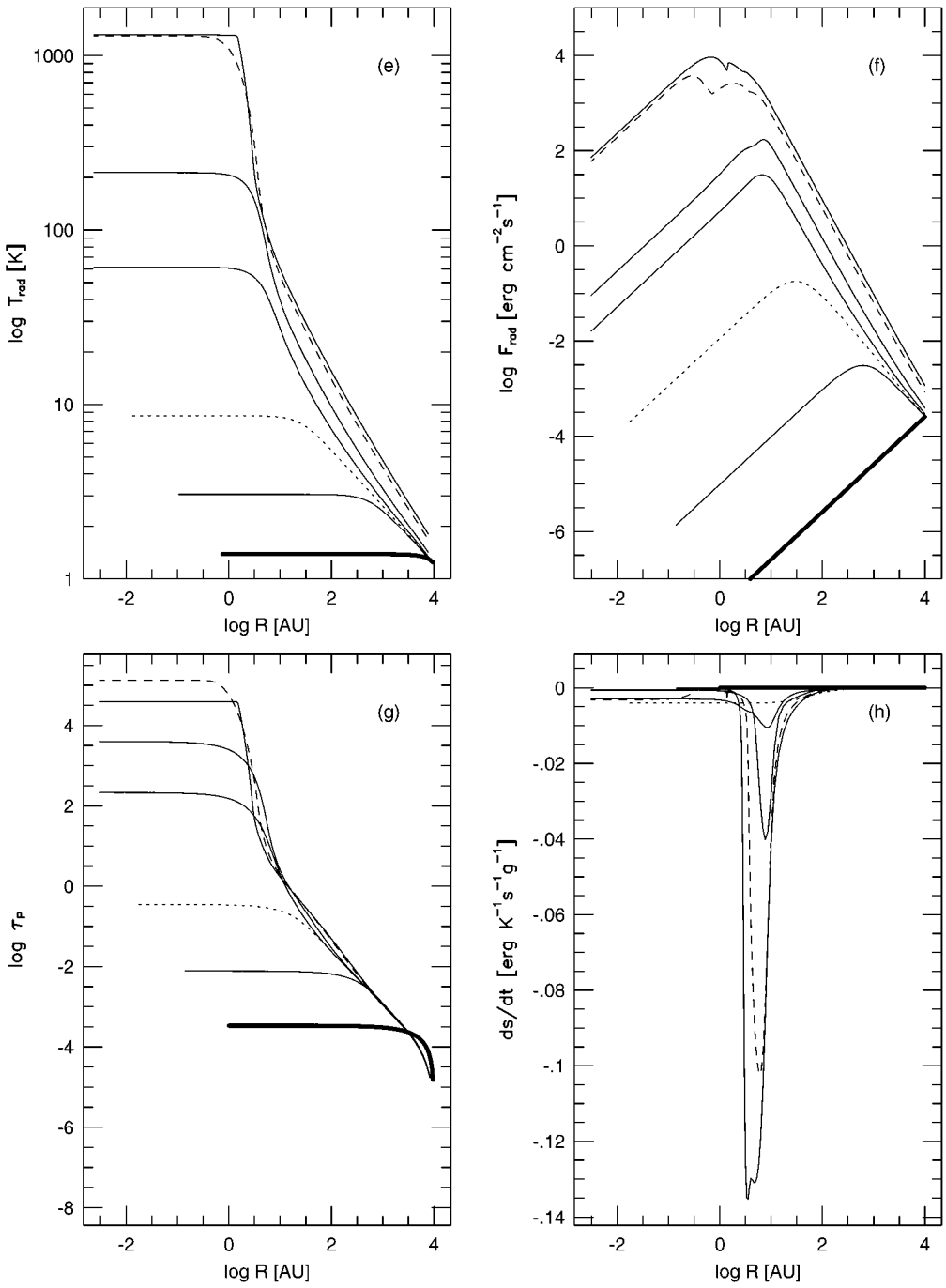

FIG. 1—*Continued*

which reads 0.05 $M_\odot$ in the final stage of this calculation. This value is consistent with the result by Boss & Myhill (1992). Figure 2 shows more directly that the mass of the first core, which is indicated by the peak in the velocity distribution and the drop in the density distribution, is increasing up to $\sim 0.05\, M_\odot$.

The dashed lines represent the stage when the dust grains begin to evaporate in the central region. The complicated behavior in the radiative flux for $R < 1$ AU is caused by the sudden decrease of the opacity due to the dust vaporization.

The evolution of the spectral energy distribution (SED) is presented in Figure 3. The panels except the lower right panel suppose observations with different beam sizes of the telescopes. These panels show that evolutionary changes would be detected more clearly by observations with smaller beam sizes. This is because a finer beam can concentrate the field of view on a more restricted region in the center of the collapsing cloud core, where the evolution is proceeding most dramatically. The spectral evolution for fine beams is mainly due to the developing density distribution and is not due to the temperature evolution. Indeed, the SEDs give us little information about the rapid increase of temperature in the first core. The lower right panel in Figure 3 gives us an answer to the question of why SEDs are not aware of the existence of the hot central core. The first core of $T \sim 2000$ K radiates mostly in the frequency range near $\nu \sim 10^{13}$ Hz, at which $R(\tau = 1) > 100$ AU, while the size of the first core is only a few AU. An observer

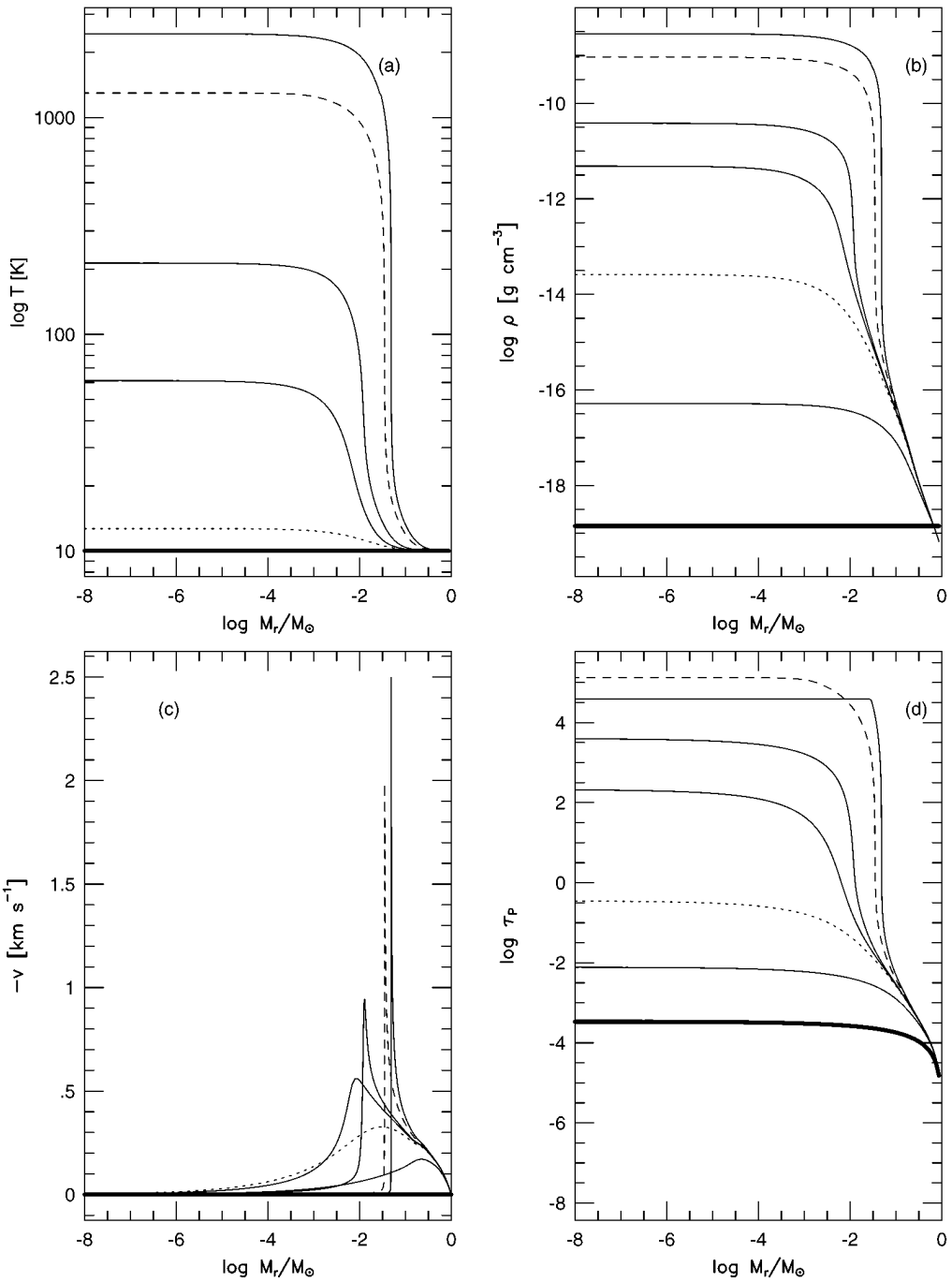

FIG. 2.—Evolutionary sequences for a typical case (model M1a) as functions of mass. See also the legend of Fig. 1. The figure depicts (*a*) temperature, (*b*) density, (*c*) infall velocity, and (*d*) Planck mean optical depth.

therefore cannot see through down to the surface of the first core, but only observes the cold envelope of $T \sim 20$ K.

Second, we examine the physical processes that determine the thermal evolution from the isothermal collapse to the adiabatic contraction. Figure 4 illustrates the thermal evolution at the center of the collapsing cloud core for the same model as above (i.e., M1a in Table 1). In Figure 4 the evolution proceeds from left to right as the central density increases monotonically with time.

Initially the radiative cooling rate, $\Lambda_{\rm th} \equiv 4\pi\kappa_P B$, and the cosmic ray heating rate, $\epsilon_{\rm CR}$, are balanced, while the radiative heating rate, $c\kappa_E E$, and the gas compressional heating rate, $\Gamma_g \equiv (p/\rho)\nabla \cdot \boldsymbol{v}$, are considerably smaller as compared to them. Here the heating and cooling rates are evaluated per unit mass. As the cloud core collapses, Γ_g shows an increase proportional to the square root of the density for $\rho_c \gtrsim 10^{-17}$ g cm^{-3}, which is accounted for in equation (13). The slight disturbance of the compressional heating rate appearing in $\rho_c \lesssim 10^{-17}$ g cm^{-3} is caused by the homogeneous and static initial condition, which is far from the similarity solution. The radiative heating rate also increases with the central density, reflecting that the dust grains (the emitter of photons) are being concentrated into the central region.

In principle, the increase of temperature due to the compressional heating can raise the radiative cooling rate

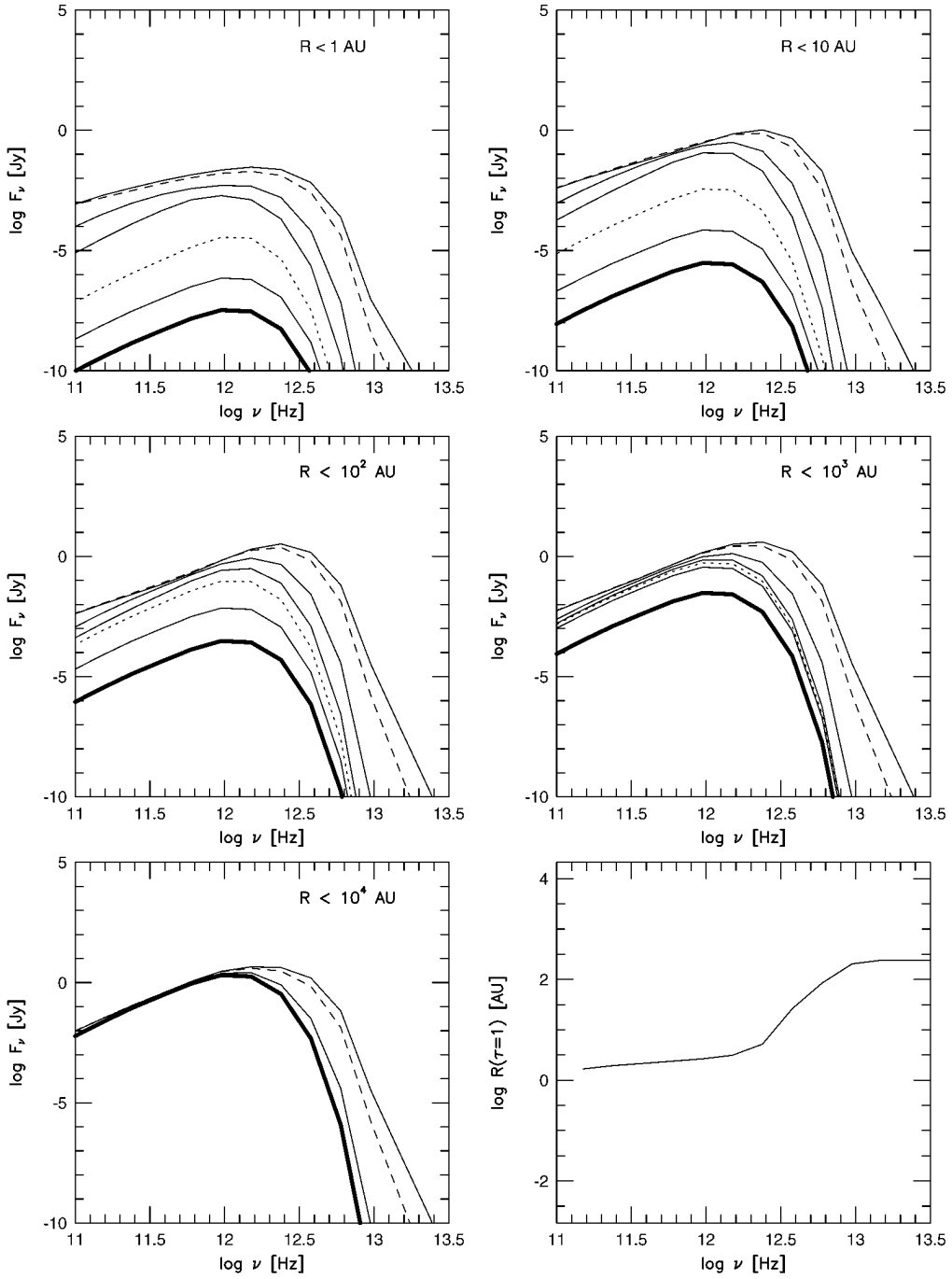

FIG. 3.—Evolution of spectral energy distributions (SEDs) for model M1a. Panels except the lower right show SEDs integrated over the different beam sizes of an imaginary telescope. A beam size corresponds to a concentric circle of the radii indicated in the panel. The lower right panel shows the radius at which the optical depth measured from an observer reaches unity as a function of frequency.

because $\Lambda_{\rm th}$ has a positive dependence on T. For $\rho_c < 10^{-14}$ g cm^{-3}, however, the radiative cooling rate is much larger than the compressional and radiative heating rates, and $\Lambda_{\rm th}$ is a very steep function of temperature, so that a very slight increase of temperature is enough to compensate for the compressional heating. Thus the gas stays isothermal for $\rho_c < 10^{-14}$ g cm^{-3}.

When Γ_g gets sufficiently close to $\Lambda_{\rm th}$ at $\rho_c \sim 10^{-14}$ g cm^{-3}, the radiative cooling no longer keeps the cloud core isothermal against the compressional heating. Thus, the central temperature T_c departs from $T_{\rm init}$. At $\rho_c \sim 10^{-12}$ g cm^{-3} the radiative heating rate overtakes $\Lambda_{\rm th}$, when the optical depth to the thermal radiation reaches the order of unity. (Note that the condition "the radiative heating rate is approximately the radiative cooling rate" corresponds to $\tau \gtrsim 1$ only when the radiation field has no external contributions.) Further evolution occurs without efficient cooling and thus enters the adiabatic phase. The central temperature increases linearly in the log T_c–log ρ_c plane with the gradient of $\sim 2/3$ for $\rho_c \gtrsim 10^{-12}$ g cm^{-3}. This behavior proves that the isothermal collapse has been replaced by the adiabatic contraction because in adiabatic evolutions $d \log T/d \log \rho$ equals $\gamma - 1$, with $\gamma - 1 = 2/3$ for $\gamma = 5/3$. The adiabatic evolution decelerates the self-gravitational

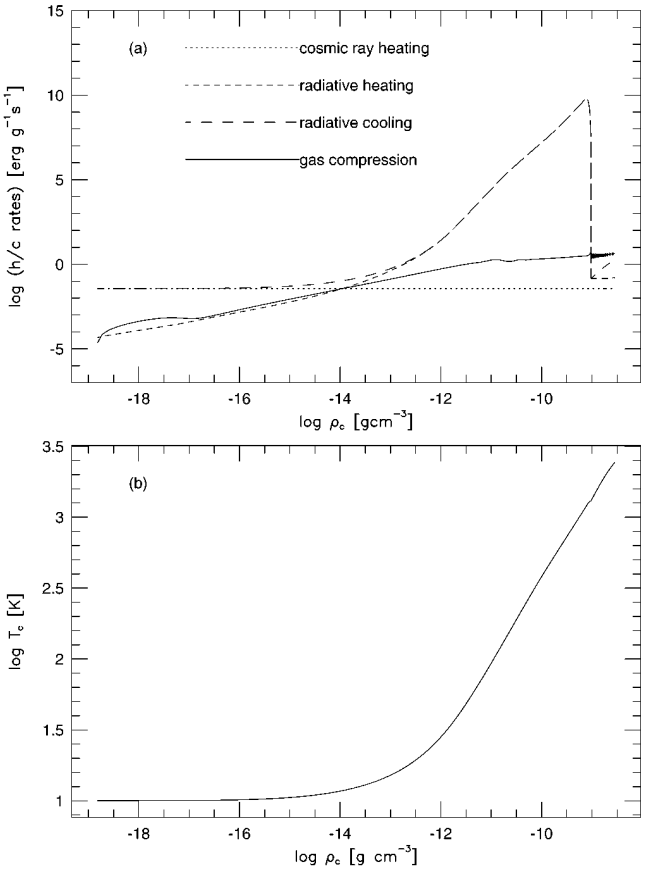

FIG. 4.—Thermal evolution at the center of a collapsing cloud core for model M1a. (*a*) The heating and cooling rates per unit mass as functions of the central density. The evolution proceeds from left to right. (*b*) The log T–log ρ plane.

collapse and thus diminishes the value of $d \ln \Gamma_g / d \ln \rho_c$ to less than 1/2. The abrupt drops of the radiative heating and cooling rates at $\rho_c \sim 10^{-9}$ are due to the dust vaporization.

It can be shown that our results are consistent with past works. In Larson (1969) the "initial" mass and radius of the first core when the central density reaches 170 K are 10^{31} g and 6×10^{31} g cm^{-3}, respectively, which are roughly equal to our results at a corresponding evolutionary stage (see Fig. 1). Figure 4 shows good agreement with Figure 3 in Boss (1988), who performed three-dimensional RHD calculations with the three-dimensional Eddington approximation. Moreover, his result for the lower opacity model is also quite similar to our lower opacity model (model M1c, see § 6.4 and Fig. 9). These imply that our results in spherical symmetry would be helpful for investigations in general symmetry.

5.2. *Characteristic Densities*

The characteristic central density when Γ_g reaches $\Lambda_{\rm th}$ can be evaluated as follows. The explicit expressions of $\Lambda_{\rm th}$ and Γ_g are

$$\Lambda_{\rm th} = 4\kappa_P \sigma T^4 , \quad \Gamma_g = -p \frac{d}{dt}\left(\frac{1}{\rho}\right) . \tag{12}$$

The central density evolves with the dynamical timescale $\sim (4\pi G\rho)^{-1/2}$ and so that d/dt can be replaced by $C_1 (4\pi G\rho^3)^{1/2} (d/d\rho)$, where C_1 is a dimensionless constant of the order of unity ($C_1 = 1.5$ for the Larson-Penston solution). Thus, the gas compressional heating rate for self-gravitational collapse becomes

$$\Gamma_g = C_1 c_s^2 \sqrt{4\pi G\rho} , \tag{13}$$

where c_s is the isothermal sound speed for the initial temperature. Our numerical calculations implied that $C_1 = 1.0$ provides a good approximation for Γ_g. Equating $\Lambda_{\rm th}$ with Γ_g in equation (12) using equation (13), one has the central density when $\Lambda_{\rm th} = \Gamma_g$ as

$$\rho_{\Lambda=\Gamma} = 1.4 \times 10^{-14} \text{ g cm}^{-3} \left(\frac{C_1}{1.0}\right)^{-2} \times \left(\frac{\kappa_P}{1.6 \times 10^{-2} \text{ cm}^2 \text{ g}^{-1}}\right)^2 \left(\frac{T_{\rm init}}{10 \text{ K}}\right)^6 . \tag{14}$$

We regard this analytic expression as the characteristic density for the violation of isothermality in the optically thin case. On the other hand, the condition that the optical depth of the thermal emission becomes unity ($\tau_{\rm cc} \sim 1$) also defines another characteristic density. For the purpose of calculating the optical depth of the cloud, we approximate the density distribution as $\rho = \rho_c (r/R_b)^{-n}$, where $n = 0$ inside of $r = R_b$ and $n = 2$ outside. R_b is the boundary between the inner and the outer regions, and approximately accords with the Jeans length corresponding to the current central density. That is,

$$R_b = C_2 \frac{2\pi c_s}{\sqrt{4\pi G\rho_c}} \tag{15}$$

where a dimensionless constant C_2 is 0.75 by comparison with numerical results. $\tau_{\rm cc}$ is then calculated as follows.

$$1 \sim \tau_{\rm cc} = \int_0^{R_{\rm cc}} \kappa\rho \, dr \sim \int_0^{R_b} \kappa\rho_c \, dr + \int_{R_b}^{R_{\rm cc}} \kappa\rho_c \left(\frac{r}{R_b}\right)^{-2} dr = \kappa\rho_c R_b \left(2 - \frac{R_b}{R_{\rm cc}}\right) .$$

Neglecting $R_b/R_{\rm cc}$ in the last term, since it is much less than unity,

$$\kappa\rho_c R_b = \tfrac{1}{2} . \tag{16}$$

Combining equations (15) and (16), we have

$$\rho_{\tau\sim 1} = 4.3 \times 10^{-13} \text{ g cm}^{-3} \times \left(\frac{C_2}{0.75}\right)^{-1} \left(\frac{\kappa_P}{1.6 \times 10^{-2} \text{ cm}^2 \text{ g}^{-1}}\right)^{-2} \left(\frac{T_{\rm init}}{10 \text{ K}}\right)^{-1} . \tag{17}$$

Equations (14) and (17) are roughly consistent with the results by Inutsuka & Miyama (1997), who derived them for a cylindrical collapse.

Note that $\rho_{\Lambda=\Gamma}$ and $\rho_{\tau\sim 1}$ depend sensitively both on the initial temperature and on the opacity. Therefore the thermal evolution during the first collapse under other circumstances can be quite different. We shall discuss the effect of different initial temperature and opacity in § 6.

We also note that the condition of $\tau \sim 1$ does not trigger the adiabatic phase in cases where the compressional heating rate is still considerably small compared to the radiative cooling rate when ρ_c reaches $\rho_{\tau\sim 1}$, because the actual cooling rate by radiation, $4\pi\kappa_P B - c\kappa_E E$, is still larger than Γ_g even when $4\pi\kappa_P B \sim c\kappa_E E$ in such cases. We will consider these situations in § 6.3.2, where another criterion is proposed instead of equations (14) and (17).

6. PROPERTIES OF THE FIRST CORE

In this section we define the mass and radius of the first core from the numerical results. The radius and mass of the first core have significance for determination of the accretion luminosity, which can relate the theoretical results with observational data. In the present paper we focus our investigation on estimating the size, mass, and accretion luminosity of the first core and discuss possible interpretations of observational evidences, taking SEDs as well into consideration.

6.1. *Definitions of the Core Radius*

First we argue how to define the radius of the first core, $R_{\rm fc}$. Three different (i.e., dynamical, thermodynamical, and geometrical) definitions are examined as follows.

1. $R_{\rm fc}$ is defined where the gas pressure is balanced with the ram pressure of the infalling envelope.
2. $R_{\rm fc}$ is defined at the position of the peak of ds/dt, where s is the specific entropy (see Fig. 1*h*).
3. $R_{\rm fc}$ is considered as the position where $d \ln \rho / d \ln r$ has the maximum value (see Fig. 1*b*).

Figure 5*a* shows $R_{\rm fc}$ in each definition as a function of ρ_c. The lines converge after the first core is formed ($\rho_c \gtrsim 10^{-11}$ g cm^{-3}) and indicate a few AU for $R_{\rm fc}$. We consider that it is most desirable to adopt definition 1 [$R_{\rm fc} \equiv r(P_{\rm gas} = P_{\rm ram})$], since it shows an intermediate value among the three and is in the best accordance with the analytical prediction estimated in § 7.1.

In the remainder of this section, the dependences of $R_{\rm fc}$ on the mass, initial temperature, and opacity are argued. The model parameters are tabulated in Table 1. In each model the calculation is performed until the central temperature reaches $\sim$2000 K, because at this temperature the first collapse should actually have been succeeded by the second collapse, which is not a subject in this paper.

6.2. *Dependence on Cloud Mass*

We present here the radii of the first core for the parent cloud cores of different masses ($M_{\rm cc}$). Models are denoted by M2a, M3a, and M4a for $M_{\rm cc} = 0.1\ M_\odot$, $0.3\ M_\odot$, and $3M_\odot$, respectively, as well as model M1a for $M_{\rm cc} = 1\ M_\odot$. The radius of the first core in each model is defined according to definition 1 in § 6.1 and is plotted in Figure 5.

Interestingly, $R_{\rm fc}$ as a function of ρ_c is not sensitive to $M_{\rm cc}$. That is, $R_{\rm fc}$ does not depend on the initial density and the size of the parent cloud core. Consequently, the mass of the first core also does not depend on the mass of its parent cloud core. A qualitative explanation of the result is briefly summarized as follows. A given mass of the parent cloud

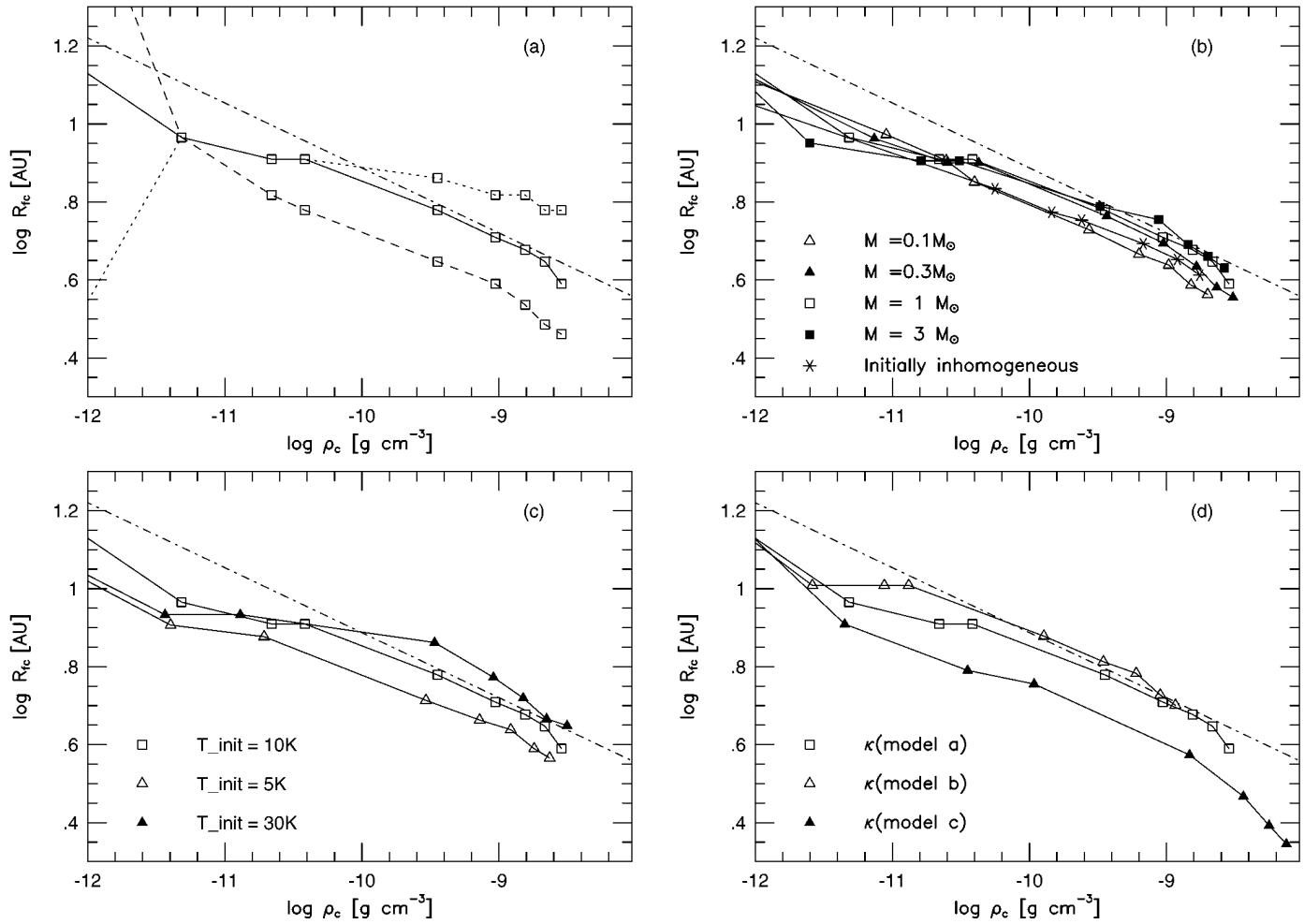

FIG. 5.—Radius of the first core, $R_{\rm fc}$. (*a*) Various definitions for $R_{\rm fc}$ are shown. The definition $R(P_{\rm gas} = P_{\rm ram})$ is represented by the solid line, $R(d \ln \rho / d \ln r = \max)$ by the dashed line, and $R(ds/dt = \max)$ by the dotted line. $R(P_{\rm gas} = P_{\rm ram})$ is adopted as $R_{\rm fc}$ in the following panels: (*b*) $R_{\rm fc}$ for different masses of the parent cloud core and for an initially inhomogeneous density distribution, (*c*) for different initial temperatures, and (*d*) for different opacities. See text for denotation of models *a*, *b*, and *c*. The analytical estimation for $R_{\rm fc}$ assuming 10 K for $T_{\rm init}$ and 10^{-13} g cm^{-3} for $\rho_{\rm ad}$ is shown as well (*dot-dashed lines*).

core determines the initial density and its radius. In the isothermal phase the density evolution of the collapsing cloud core "forgets" its initial condition and develops into centrally peaked density profile (which resembles the Larson-Penston solution) in the sound crossing time over the entire cloud core (as noted also by Bodenheimer & Sweigart 1968). Therefore the evolution, regardless of mass, converges to the sequence that is determined uniquely by the initial temperature. The physical processes that change the isothermal phase into the adiabatic phase are affected only by the initial temperature and opacity, according to equations (14) and (17), and thus the properties of the first core are affected by $T_{\rm init}$ and κ_P but are independent of the mass of the cloud core.

For comparison, we carried out a calculation with an inhomogeneous initial density distribution. We provided an isothermal equilibrium configuration with the central density of 10^{-17} g cm^{-3} as the initial density distribution, for which the outer radius truncated at 10^4 AU. The mass of the cloud is 0.87 $M_\odot$. The resultant value of $R_{\rm fc}$ shows no significant differences from the other cases, as seen in Figure 5*b*, which supports the forgetful nature of collapsing cloud cores.

6.3. *Dependence on Initial Temperature*

The Taurus-Auriga molecular cloud has a typical temperature of 10 K, which motivated us to choose the initial temperature of $T_{\rm init} = 10$ K as a typical value. However, the existence of massive stars in the neighborhood of star-forming clouds would raise initial temperatures for the collapse of cloud cores such as in the Orion clouds. In contrast, the interior of cloud cores may well have a lower temperature than the typical value of the entire cloud because visual or UV photons from neighboring stars would not reach deep inside cloud cores. Indeed, the value of 9.6×10^{-2} ergs s^{-1} g^{-1} for $\epsilon_{\rm CR}$, which was found to be required to sustain the initial cloud core at $T = 10$ K, is larger by 2 orders of magnitude than the typical cosmic ray heating rate.

Hence, model calculations for $T_{\rm init} = 5$ K (model C1a) and 30 K (model H1a) are carried out to be compared to the typical case of $T_{\rm init} = 10$ K. The other conditions are the same as model M1a.

6.3.1. *Case for* $T_{\rm init} = 5$ K

Equation (14) claims that $\rho_{\Lambda=\Gamma}$ decreases quite sensitively with decreasing initial temperature. The Planck mean opacity, moreover, has a lower value for a lower initial temperature, which makes $\rho_{\Lambda=\Gamma}$ diminish with $T_{\rm init}$ more sensitively. For $T_{\rm init} = 5$ K, we have

$$\rho_{\Lambda=\Gamma} = 8.8 \times 10^{-18} \text{ g cm}^{-3} ,$$

noting that $\kappa_P(5\text{ K})$ is calculated to be 3.2×10^{-3} cm^2 g^{-1}. It is found that lowering $T_{\rm init}$ by a factor of 2 yields a $\rho_{\Lambda=\Gamma}$ that is lower by 3 orders of magnitude. In contrast, $\rho_{\tau\sim1}$ has a negative dependence upon the initial temperature (see eq. [17]). For $T_{\rm init} = 5$ K one finds

$$\rho_{\tau\sim1} = 2.2 \times 10^{-11} \text{ g cm}^{-3} .$$

In this case $\rho_{\tau\sim1}$ exceeds $\rho_{\Lambda=\Gamma}$ by 6 orders of magnitude, in contrast to the case of $T_{\rm init} = 10$ K, where they are comparable to each other. This contrast causes a large difference in thermal history between the two cases.

Figure 6 illustrates the thermal evolution for $T_{\rm init} = 5$ K. One can see that the isothermal phase ceases rather early,

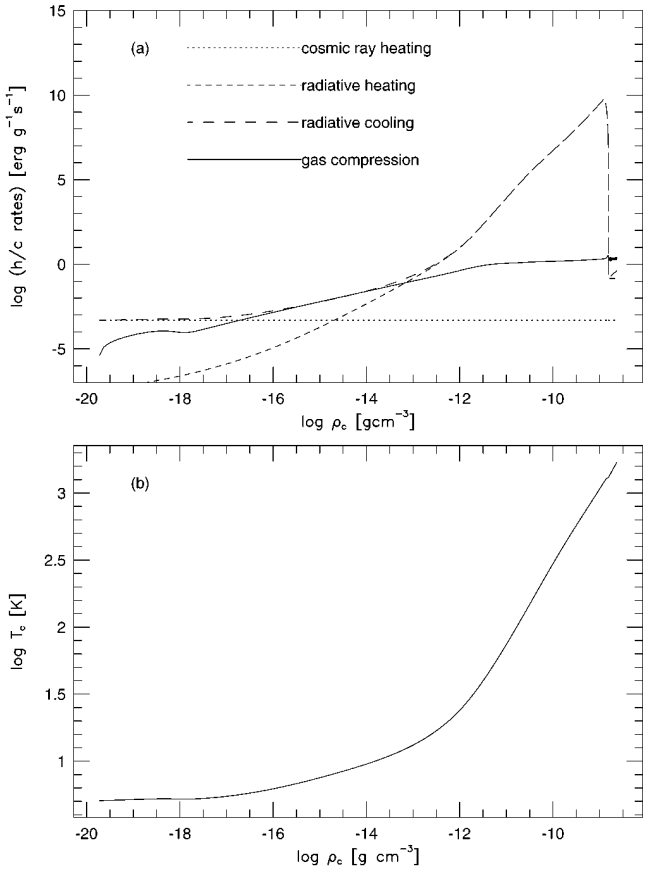

FIG. 6.—Thermal evolution at the center of a collapsing cloud core for model C1a ($T_{\rm init} = 5$ K). See also the legend of Fig. 4.

when ρ_c reaches $\rho_{\Lambda=\Gamma}$, and that the central temperature increases gradually during a long transitional phase before the adiabatic stage is entered when ρ_c exceeds $\rho_{\tau\sim1}$. In the transitional phase, where $\rho_{\Lambda=\Gamma} < \rho_c < \rho_{\tau\sim1}$, the compressional heating rate attempts to dominate the radiative cooling rate, but is pursued immediately by it in response to the raised central temperature. Consequently Γ_g and $\Lambda_{\rm th}$ are almost balanced with each other as they increase gradually with ρ_c before the optical depth becomes unity.

The isothermal approximation, which many theoretical works suppose for collapse calculations, is often considered to be valid when $\rho_c < \rho_{\tau\sim1} \sim 10^{-13}$ g cm^{-3}. However, under the situations where $\rho_{\Lambda=\Gamma} \ll \rho_{\tau\sim1}$ as in model C1a, the transitional phase breaks the isothermal condition far before the adiabatic stage begins, which implies that the isothermal approximation is not so valid even for $\rho_c < \rho_{\tau\sim1}$. This aspect is critical especially for cylindrical collapses, where even a slight hardening of the isothermal equation of state can decelerate the gravitational collapse (Inutsuka & Miyama 1997).

6.3.2. *Case for* $T_{\rm init} = 30$ K

If the cloud core is surrounded by energy sources such as OB stars, the temperature of the cloud can be larger from the beginning of the collapse. Indeed, cloud cores in the Orion clouds should be exposed to hard radiation fields, and the average temperature of the Orion clouds is considerably higher than that of dark clouds. Therefore the calculation with higher initial temperature should be instructive for the understanding the effect of different environments. Thus in model H1a, we have removed $\epsilon_{\rm CR}$

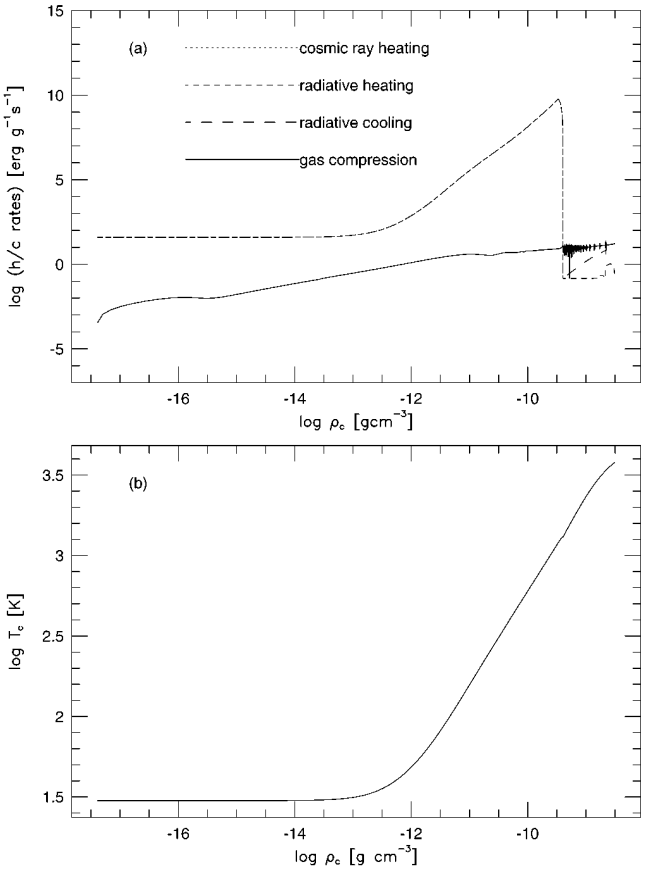

FIG. 7.—Thermal evolution at the center of a collapsing cloud core for model H1a ($T_{\rm init} = 30$ K). This is a case where $\epsilon_{\rm CR}$ is absent and the incident radiation field is present. Note the difference in panel (*a*) from the other models. See also the legend of Fig. 4.

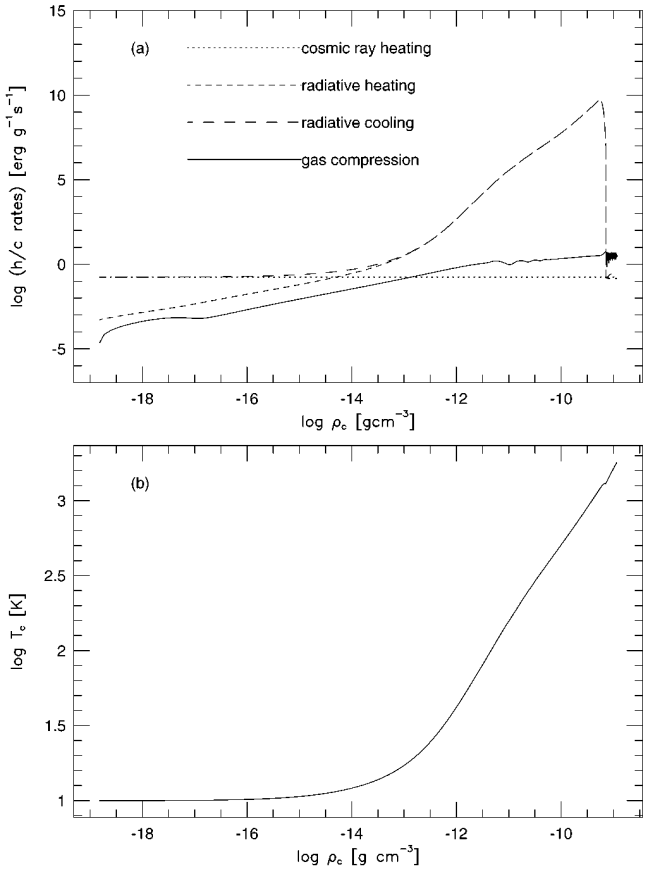

FIG. 8.—Thermal evolution at the center of a collapsing cloud core for model M1b (larger opacity). See also the legend of Fig. 4.

and introduced incident blackbody radiation of $T_{\rm init}$ instead (i.e., case 2 in § 4.2) for $T_{\rm init} = 30$ K. The results are shown in Figure 7.

Substituting $T_{\rm init} = 30$ K and $\kappa_P(T = 30\ {\rm K}) = 2.1 \times 10^{-1}$ cm^2 g^{-1} in equations (14) and (17), we have

$$\rho_{\Lambda=\Gamma} = 1.8 \times 10^{-9}\ {\rm g\ cm^{-3}}\ ,$$
$$\rho_{\tau\sim 1} = 8.3 \times 10^{-16}\ {\rm g\ cm^{-3}}\ .$$

In contrast to the result of $T_{\rm init} = 5$ K, $\rho_{\tau\sim 1}$ is greatly exceeded by $\rho_{\Lambda=\Gamma}$. The collapsing cloud experiences $\tau \sim 1$ at the early stage in the evolution far before the radiative cooling rate is balanced with the gas compressional heating rate. However, Figure 7*b* shows isothermal evolution even when $\rho_c > \rho_{\tau\sim 1}$. Hence $\rho_{\Lambda=\Gamma}$ and $\rho_{\tau\sim 1}$ lose their roles as the criterion between the isothermal and adiabatic phases. The adiabatic phase is set up when the compressional heating rate, Γ_g, becomes comparable to the cooling rate due to the radiative diffusion, $\Lambda_{\rm dif}$. If the internal energy density of material per unit mass, e, is larger than the radiation energy density per unit volume, E, $\Lambda_{\rm dif}$ can be written as $(E/\rho)/t_{\rm dif}$, otherwise $\Lambda_{\rm dif}$ equals $e/t_{\rm dif}$, where $t_{\rm dif} \equiv \kappa_P \rho l^2/c$ denotes the radiative diffusion time with l for the length scale of the system. Thus the criterion is now expressed by

$$\Gamma_g = \Lambda_{\rm dif} \equiv \min\left(e, \frac{E}{\rho}\right)\frac{1}{t_{\rm dif}}\ , \tag{18}$$

for low-mass star formation, where $e \gg E/\rho$, min $(e, E/\rho)$ is always replaced by E/ρ. (Otherwise it should be replaced by e, which leads eq. [18] into a simpler criterion $t_{\rm dyn} = t_{\rm dif}$.)

Substituting $2R_b$ for l by recalling the argument above equation (17), one has

$$\Lambda_{\rm dif} = \frac{\sigma T^4}{\kappa_P \rho^2 R_b^2}\ , \tag{19}$$

where $E \equiv aT^4$ has been used since we consider the situation where the optical depth has already exceeded unity. Combining equation (18) with equations (13), (15), and (19), we have

$$\rho_{\rm dif} = 1.2 \times 10^{-13}\ {\rm g\ cm^{-3}} \left(\frac{C_1}{1.0}\right)^{-2/3}\left(\frac{C_2}{0.75}\right)^{-4/3} \times \left(\frac{\kappa_P}{1.6 \times 10^{-2}}\right)^{-2/3}\left(\frac{T_{\rm init}}{10\ {\rm K}}\right)^{4/3}\ . \tag{20}$$

For $T_{\rm init} = 30$ K and $\kappa_P(30\ {\rm K}) = 2.1 \times 10^{-1}$ cm^2 g^{-1},

$$\rho_{\rm dif} = 9.2 \times 10^{-14}\ {\rm g\ cm^{-3}}\ .$$

Figure 7*a* clearly shows the turning point between the isothermal and adiabatic phases at $\rho_c = \rho_{\rm dif}$. In great contrast to the case of $T_{\rm init} = 5$ K, where the transitional phase interrupts the isothermal stage before $\tau \sim 1$, the isothermal phase lasts even after the optical depth exceeds unity.

6.4. *Dependence on Opacity*

We consider here the influences caused by the ambiguity of the dust opacity for submillimeter and millimeter wavelengths. As described in § 4.3, the three models of different opacities are examined. We provide models M1b and M1c, that correspond to models *b* and *c* in § 4.3.

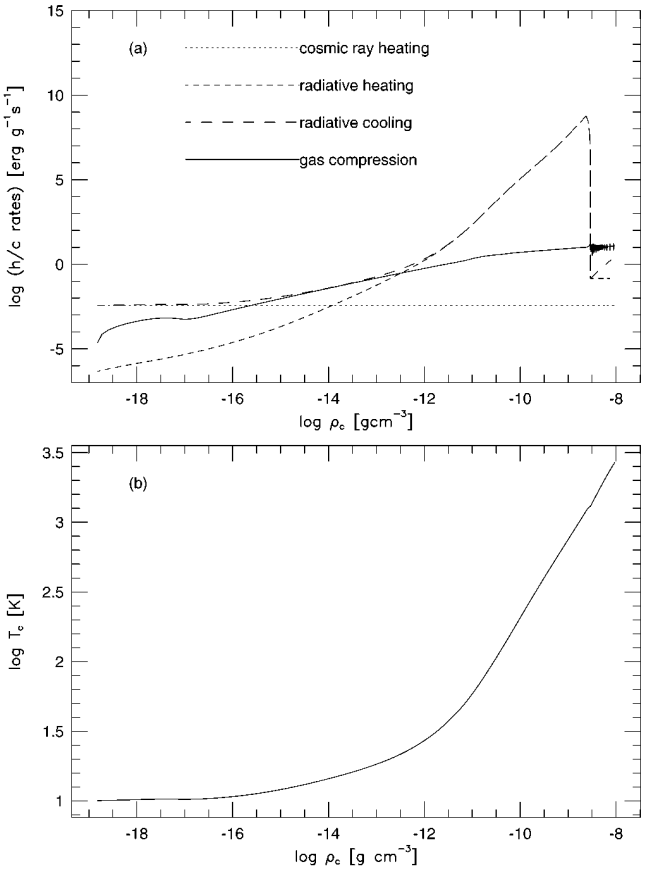

FIG. 9.—Thermal evolution at the center of a collapsing cloud core for model M1c (smaller opacity). See also the legend of Fig. 4.

The opacity of model *b* gives $\kappa_P = 7.7 \times 10^{-2}$ cm^2 g^{-1}, which is larger by a factor of 5 than model *a*. Equations (14) and (17) for this case yield

$$\rho_{\Lambda=\Gamma} = 3.2 \times 10^{-13} \text{ g cm}^{-3} ,$$

$$\rho_{\tau\sim 1} = 1.9 \times 10^{-14} \text{ g cm}^{-3} .$$

Considering $\rho_{\tau\sim 1} < \rho_{\Lambda=\Gamma}$, one might prefer

$$\rho_{\text{dif}} = 4.2 \times 10^{-14} \text{ g cm}^{-3}$$

as the central density where the isotherm is connected with the adiabat. However, under situations where $\rho_{\tau\sim 1}$ is close enough to $\rho_{\Lambda=\Gamma}$, as in this case, $\rho_{\tau\sim 1}$ represents the critical density because the compressional heating rate is no longer negligible when the optical depth reaches unity as seen in Figure 8.

For model *c*, where the dust-to-gas ratio is decreased by a factor of 10 from model *a*, κ_P equals 1.6×10^{-3} cm^2 g^{-1}, which is of course a tenth of the value of model *a*. Equations (14) and (17) give

$$\rho_{\Lambda=\Gamma} = 1.4 \times 10^{-16} \text{ g cm}^{-3} ,$$

$$\rho_{\tau\sim 1} = 4.3 \times 10^{-11} \text{ g cm}^{-3} .$$

Figure 9 shows that the transitional phase appears again where $\rho_{\Lambda=\Gamma} < \rho_c < \rho_{\tau\sim 1}$ (see § 6.3.1). It would be worth noting that the transitional phase also appears for the lower opacity model in Figure 3 in Boss (1988).

7. DISCUSSION

In the previous section, we noted the importance of determining the radius and mass of the first core and defined them in the numerical results. We will show in this section that they can be derived from semianalytical considerations. Possible interpretations of the observational YSOs are also discussed, on the basis of the accretion luminosities and SEDs in our results.

7.1. *Analytical Derivation of the Core Radius*

We approximate the first core as a polytropic sphere in equilibrium. Although the first core is not strictly isentropic, one finds that this approximation provides an excellent prediction of the radius of the first core. The equilibrium configurations are expressed by the Lane-Emden equation

$$\frac{1}{\xi^2}\frac{d}{d\xi}\left(\xi^2 \frac{d\theta}{d\xi}\right) = -\theta^n , \tag{21}$$

where we follow the standard notation of Chandrasekhar (1967). In the present calculations the ratio of specific heats, γ, is fixed to 5/3, i.e., $n = 1.5$. The radius of a polytropic sphere in equilibrium, R_{LE}, is

$$R_{\text{LE}}(\rho_c) = \left[\frac{(n+1)K}{4\pi G}\,\rho_c^{1/n-1}\right]^{1/2} \xi_1 , \tag{22}$$

where $\xi_1 = 3.65375$ for $n = 1.5$ (Chandrasekhar 1967) and $K \equiv p/\rho^\gamma$, which relates with the entropy that the system has. One immediately obtains K as follows:

$$K = c_{s0}^2\, \rho_{\text{ad}}^{1-\gamma} , \tag{23}$$

where c_{s0} is the sound speed at the initial isothermal phase and ρ_{ad} is defined as the intersection of extrapolated lines of the isotherm and the adiabat in the log ρ–log T plane (as illustrated in Fig. 10). The log ρ–log T planes of numerical solutions are shown in Figures 4, 6, 7, 8, and 9, which read the typical value of 10^{-13} g cm^{-3} for ρ_{ad} as tabulated in Table 1. Substituting equation (23) into equation (22), one obtains the analytical description of R_{fc} as follows.

$$R_{\text{fc}}(\rho_c) = 5.3 \text{ AU} \left(\frac{\rho_c}{10^{-9} \text{ g cm}^{-3}}\right)^{-1/6} \left(\frac{T_{\text{init}}}{10 \text{ K}}\right)^{1/2} \times \left(\frac{\rho_{\text{ad}}}{10^{-13} \text{ g cm}^{-3}}\right)^{-1/3} . \tag{24}$$

Figure 5 delineates $R_{\text{fc}}(\rho_c)$ in equation (24) (*dot-dashed line*), with T_{init} and ρ_{ad} set to be 10 K and 10^{-13} g cm^{-3}, respectively. One will find that the analytical prediction is in excellent accordance with the numerical results.

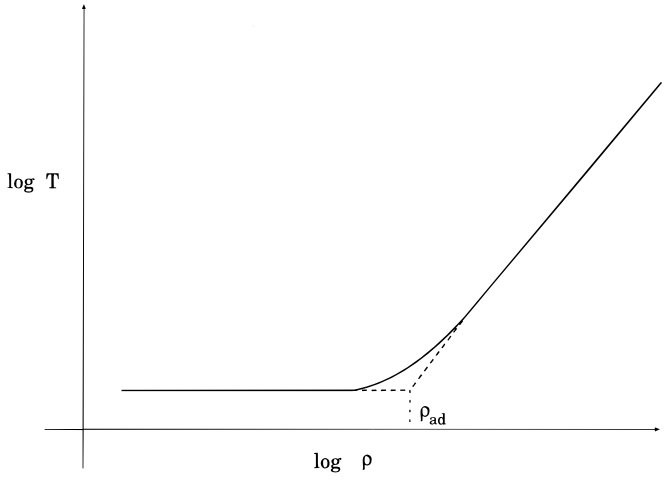

FIG. 10.—Definition of ρ_{ad} (see text)

Apparently $\rho_{\rm ad}$ relates with $\rho_{\Lambda=\Gamma}$, $\rho_{\tau\sim1}$, and/or $\rho_{\rm dif}$. Because all of $\rho_{\Lambda=\Gamma}$, $\rho_{\tau\sim1}$, and $\rho_{\rm dif}$ depend solely on $T_{\rm init}$ and κ_P as seen in equations (14), (17), and (20), $R_{\rm fc}$ also depends only on $T_{\rm init}$ and κ_P when ρ_c is given, which supports the numerical results that $R_{\rm fc}$ is independent of the mass of the parent cloud core (see § 6.2).

Interestingly, $\rho_{\rm ad}$ seems never to depart from 10^{-13} g cm^{-3} further than an order of magnitude for any models examined here, in contrast to $\rho_{\Lambda=\Gamma}$ and $\rho_{\tau\sim1}$ themselves, which vary quite sensitively to the initial temperature. Moreover, considering the weak dependences of $R_{\rm fc}$ on ρ_c, $T_{\rm init}$, and $\rho_{\rm ad}$ in equation (24), one will find that the typical value of 5 AU for $R_{\rm fc}$ would be a reasonable estimate for any cases unless extreme conditions for $T_{\rm init}$ and κ_P are supposed. Indeed, Figure 5 shows that the radius of the first core converges to several AU in every model.

7.2. *Estimate of the Accretion Luminosity*

The emergent flux of the radiation is the most important quantity when we compare our results to observational data. In this section we express the total luminosity obtained from the numerical calculations, in terms of analytic expression.

So-called accretion luminosity is expressed as follows:

$$L_{\rm fc}^{\rm acc} = \frac{GM_{\rm fc}\dot{M}}{R_{\rm fc}}\,, \tag{25}$$

where $M_{\rm fc}$ and $\dot{M}$ are the mass of the first core and the mass accretion rate, respectively. For determining $L_{\rm fc}^{\rm acc}$, $M_{\rm fc}$ and $\dot{M}$ are estimated as follows.

$$M_{\rm fc} = 4\pi\rho_c R_{\rm fc}^3\left(-\frac{1}{\xi}\frac{d\theta_n}{d\xi}\right)_{\xi=\xi_1}\,, \tag{26}$$

$$\dot{M} = \alpha\,\frac{c_{s0}^3}{G}\,. \tag{27}$$

We define $M_{\rm fc}$ as the mass of an equilibrium polytropic sphere of the radius of $R_{\rm fc}$ in equation (26), where $[(1/\xi)(d\theta_n/d\xi)]_{\xi=\xi_1} = 5.5642\times10^{-2}$ for $n = 1.5$ (Chandrasekhar 1967). In equation (27) α is a dimensionless coefficient, which is found to be ~10 by comparison with the numerical results for model M1a. For another example, Shu (1977) found $\alpha = 0.975$ in the expansion-wave solution. This difference arises because the expansion-wave solution assumes an initially hydrostatic singular sphere in contrast to our homogeneous density distribution. Note that the mass accretion rate would become smaller with time in much later stages. This aspect will be discussed in detail in our subsequent papers.

Substituting equations (26) and (27) into equation (25), we obtain

$$L_{\rm fc}^{\rm acc} = 0.07\,L_\odot\left(\frac{\alpha}{10}\right)\left(\frac{\rho_c}{10^{-9}\ {\rm g\ cm^{-3}}}\right)^{2/3} \times\left(\frac{T_{\rm init}}{10\ {\rm K}}\right)^{5/2}\left(\frac{\rho_{\rm ad}}{10^{-13}\ {\rm g\ cm^{-3}}}\right)^{-2/3}\,. \tag{28}$$

Table 1 tabulates $L_{\rm fc}^{\rm acc}$ evaluated by equation (28) as well as the numerical result, L. By comparing $L_{\rm fc}^{\rm acc}$ with L, it is seen that equation (28) offers a reasonable approximation for the luminosities in most of the models.

7.3. *Case for $\gamma = 7/5$*

Hydrogen molecules in molecular cloud cores of ~10 K have the ratio of specific heats, γ, equal to 5/3 because rotational and vibrational levels of H_2 are not excited at low temperatures. However, the rotational degree of freedom raises the ratio of specific heats up to 7/5 before the temperature reaches several hundred kelvin (Black & Bodenheimer 1975). The calculations presented in this paper suppose $\gamma = 5/3$ throughout the evolution, for simplicity.

To study this effect, another calculation was performed under the same conditions as model M1a, except that γ is set to 7/5 instead of 5/3. We found that $R_{\rm fc}$ does not show apparent differences between the two cases, and $M_{\rm fc}$ is smaller by only a factor of 2 for $\gamma = 7/5$. These results are consistent with past works where the rotational degree of freedom was taken into account (Larson 1969; Tscharnuter & Winkler 1979). Therefore this simplified treatment for γ remains useful for this kind of study.

However, we will use a more realistic equation of state in the subsequent papers, where we consider the dissociation, ionization, and the rotational and vibrational degrees of freedom for molecules, as well as the nonideal effects of the equation of state such as the pressure ionization and the degeneracy of electrons.

7.4. *Comparison with Observations*

Our nongray radiation hydrodynamic calculations provide information on the frequency-dependent radiative flux. Recently a number of SEDs of young stellar objects became available. In this section we examine possible suggestions and interpretations of the observations from our results.

In Figure 3 we presented SEDs for the typical model, whose shapes were found to be quite insensitive to the thermal evolution in the center throughout the first collapse because the envelope is opaque. In Figure 12, the SEDs of the other models are shown. The shapes of those SEDs also do not reflect the rapid increase of the central temperature except for model M1c (unusually small opacity model). Therefore, if we rely only on the shape of the SEDs, it is difficult to distinguish cloud cores that have already formed the first (or possibly more evolved) cores from starless cores or precollapse cores. However the total luminosity should experience a considerable increase even at this early stage of the collapse that is hidden in the opaque envelope.

Ward-Thompson et al. (1994) presented SEDs and luminosities for four starless cores, on the basis of the results of a submillimeter continuum survey. Their masses are ~1–2 $M_\odot$ and are comparable with our models. The SEDs (Fig. 5 in Ward-Thompson et al. 1994) can be fitted by graybody spectra of $T\sim10$–20 K, which are quite similar to our results in Figures 3 and 12. Furthermore, the estimated luminosities of the observed starless cores, $10^{-1}\,L_\odot \lesssim L \lesssim 2\,L_\odot$, seem to be rather higher than expected for cores that have not yet experienced dynamical collapse. Indeed, Figure 11 depicts the evolutions of the luminosities, which reach at most $\sim10^{-1}\,L_\odot$ even at the end of the first collapse. These results show a relatively luminous ($\sim1\,L_\odot$) star-forming cloud core that might be recognized to have already formed the second core at the center. Therefore we suggest that the objects observed by Ward-Thompson et al. (1994) are possibly identified more naturally as young protostars that are hidden by opaque envelopes, rather than as

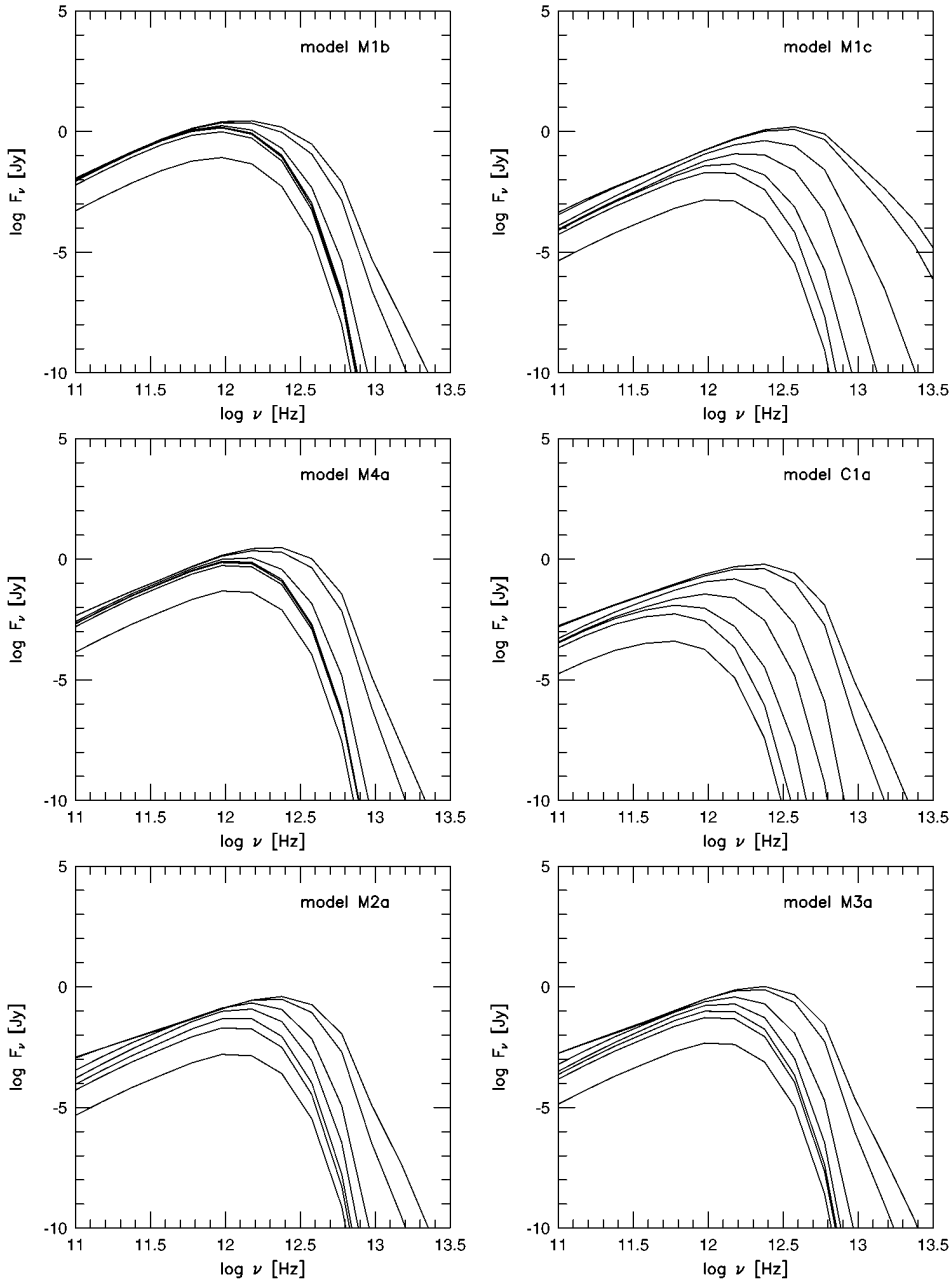

FIG. 11.—SEDs that would be observed with the beam size of 10^3 AU for different models. The SED for model H1a has been omitted because it supposes a surrounding isotropic radiation field.

preprotostellar cores as concluded by Ward-Thompson et al. (1994).

Boss & Yorke (1995) calculated SEDs at the first collapse stage, which is "class $-$I" stage by their three-dimensional numerical code. No essential discrepancy is recognized between their SEDs and ours, although the SEDs of the pole-on view by Boss & Yorke (1995) show somewhat more excess of the component of higher temperatures. (Note that the vertical axis in Figs. 1 and 2 in Boss & Yorke 1995 denotes vL_v by their definition, but F_v by our definition.) Thus the pole-on view of young stellar objects would possibly reveal the dramatic evolution at the center of the cloud cores.

8. SUMMARY

In this paper, we have investigated the properties of the first collapse and the first core by means of radiation hydrodynamic numerical calculations, supplemented by analytical considerations. Our findings are summarized as follows.

The first core finally has the mass of $\sim 0.05\ M_\odot$ and the radius of ~ 5 AU for $T_{\rm init} = 10$ K and the typical opacity. If the initial temperature and opacity are given, these values for mass and radius are uniquely determined and are independent both of the mass of the parent cloud core and of the initial density profile.

The thermal evolution at the center of a collapsing cloud core is characterized by the conditions of $\Gamma_g = \Lambda_{\rm th}$, $\tau \sim 1$, and/or $\Gamma_g = \Lambda_{\rm dif}$ (see eqs. [14], [17], and [20], respectively), depending sensitively on the initial temperature and opacity. These expressions determine how and when the early isothermal evolution changes to nearly adiabatic evolution.

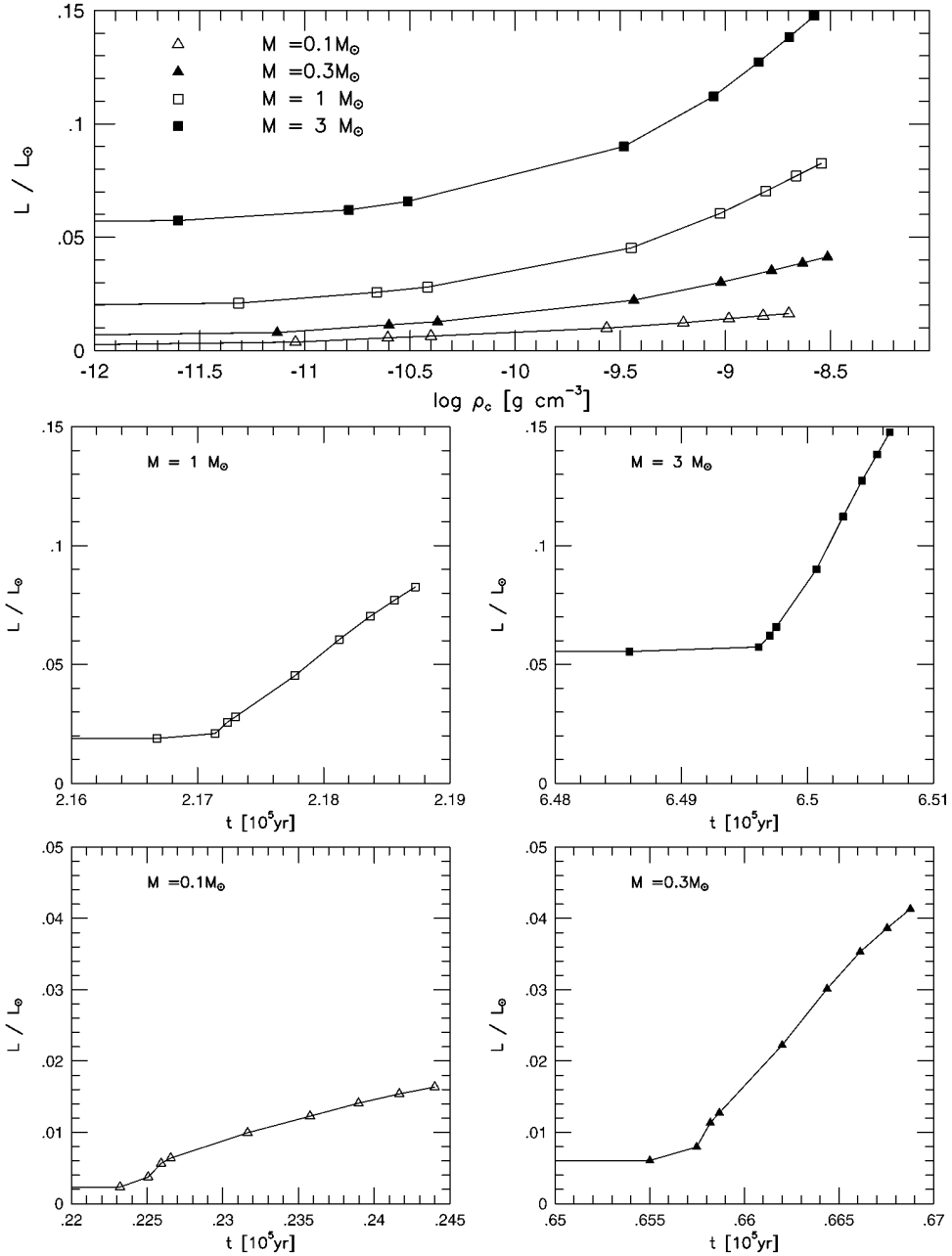

FIG. 12.—Evolutionary curves of the luminosity. L vs. ρ_c (*upper panel*) and L vs. t (*middle and lower panels*) for models M1a, M2a, M3a, and M4a. The luminosity remains at a constant value since the collapse is initiated (i.e., $t = 0$) until the luminosity begins to increase.

We have found the analytic expression for the radius of the first core (eq. [24]) and the accretion luminosity (eq. [28]) as functions of the central density. They are weakly dependent on the initial temperature and opacity. Those expressions are useful for understanding the numerical results.

The shape of the spectral energy distributions (SEDs) does not reflect the central thermal evolution of collapsing cloud cores throughout the first collapse. This result, of course, does not exclude the possibility that the first cores might be observed on the pole-on view, where the envelope material would actually be more depleted than predicted by spherically symmetrical calculations. The luminosity increases up to $\sim 0.1\ L_\odot$ at the end of the first collapse phase.

Dense cloud cores with luminosities higher than $\sim 0.1\ L_\odot$ possibly have young protostars inside the opaque envelopes, even if observations show no evidence for protostellar activities.

In the subsequent paper, we will discuss the evolution after the first collapse, in which the dissociation of hydrogen molecules causes the second collapse. The main goals will be to examine the properties of the main accretion phase and to answer the question: "When does a protostar emerges before us in near-infrared or optical light?"

The authors greatly appreciate valuable comments and help of the referee, Alan P. Boss, concerning improvements to the paper. The research of H. M. is supported in part by the Research Fellowships of the Japan Society for the Promotion of Science for Young Scientists.

APPENDIX A

THE COMPUTATIONAL METHOD IN SPHERICAL SYMMETRY

A1. THE TRANSFER EQUATION SOLVER

We solve equation (6) numerically, dropping the time derivative term, in the transfer equation solver to determine the variable Eddington factors. The transfer equation to be solved is reduced to

$$\frac{\partial j_\nu}{\partial \tau_\nu} = -h_\nu \,, \tag{A1}$$

$$\frac{\partial h_\nu}{\partial \tau_\nu} = -j_\nu + S_\nu \,, \tag{A2}$$

where

$$j_\nu \equiv \tfrac{1}{2}[I_\nu(+\mu) + I_\nu(-\mu)] \,, \tag{A3}$$

$$h_\nu \equiv \tfrac{1}{2}[I_\nu(+\mu) - I_\nu(-\mu)] \,. \tag{A4}$$

Note that an independent variable ν is noted as a subscript hereafter. Figure 13 illustrates the paths along which equations (A1) and (A2) should be integrated. The specific intensity on each point at which an integral path intersects a radial grid is integrated over μ on each ring to calculate the first three moments for radiation,

$$J_\nu = \int_0^1 j_\nu \, d\mu \,, \tag{A5}$$

$$H_\nu = \int_0^1 \mu h_\nu \, d\mu \,, \tag{A6}$$

$$K_\nu = \int_0^1 \mu^2 j_\nu \, d\mu \,, \tag{A7}$$

where μ is the direction cosine, i.e., $\mu = \cos\theta$, where θ is the angle with respect to the outward normal (see Fig. 1). The first two moments for radiation, J_ν and H_ν, correspond to the monochromatic radiation energy density and radiation flux, respectively. The third, P_ν or $(4\pi/c)\,K_\nu$, is the radiation pressure, which is the rr-component of the radiation stress tensor in spherical coordinates. Both the $\theta\theta$ and $\phi\phi$ components equal $P_\nu - (3P_\nu - E_\nu)/2$ (see MM).

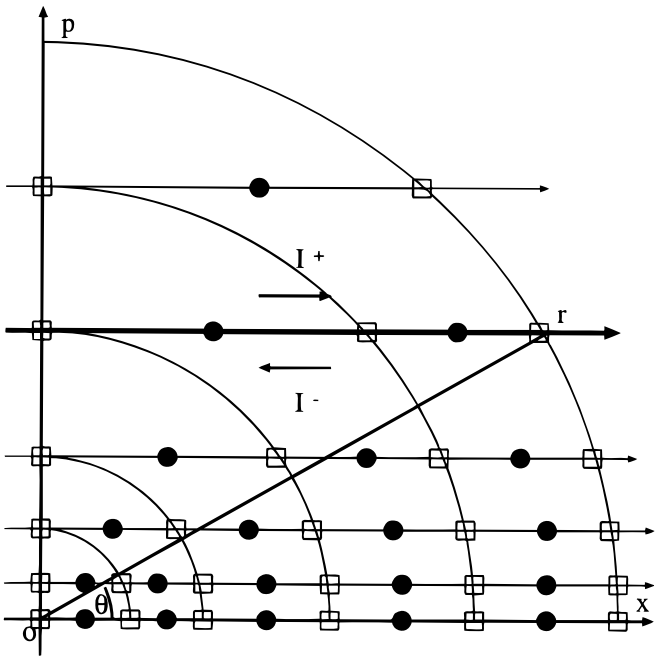

FIG. 13.—Grid employed for the discretized transfer equation. The transfer equation is integrated along the horizontal line, according to the orthodox manner in solving radiative transfer numerically in spherical symmetry. The cell-centered points (*filled circles*) and cell-faced points (*open squares*) are employed for the discretized transfer equations for j_ν and h_ν, respectively. Direction cosine, μ, is defined as $\mu = \cos\theta$, where θ is the angle between the lines ox and or.

The *scalar* variable Eddington factor is

$$f_\nu(r) = \frac{K_\nu(r)}{J_\nu(r)} .$$

When the radiation field is nearly isotropic, i.e., $I(\mu) = I_0 + I_1\,\mu$, K is found to equal $\frac{1}{3}J$ using equations (A5) and (A7). On the other hand, the streaming limit condition $I(\mu) = I\delta(\mu - 1)$ yields $K = J$. The Eddington factor thus varies between $\frac{1}{3}$ and 1, except for some special cases where f goes down below $\frac{1}{3}$, according to the degree of anisotropy of the radiation field.

We adopt the *monochromatic* transfer equation solver in our scheme. It has two advantages over the gray transfer equation solver. First, the energy mean and flux mean opacities are κ_E and κ_F for the moment equations are obtained (see § A3), whereas the Planck mean or Rosseland mean opacities are substituted in the gray approximation. Another advantage is that one can obtain SEDs directly from the monochromatic radiation fluxes. The obtained SEDs will help us to compare theoretical models to observations, as mentioned in § 2.

A2. THE MOMENT EQUATIONS SOLVER

In spherical symmetrical Lagrangian (comoving) coordinates, equations (1)–(4), (7), and (9) lead to the following (MM):

$$\frac{dr}{dt} = v , \tag{A8}$$

$$\rho = \frac{3}{4\pi}\frac{\partial M_r}{\partial (r^3)} , \tag{A9}$$

$$\frac{Dv}{Dt} = -\frac{GM_r}{r^2} - 4\pi r^2 \frac{\partial (p + Q)}{\partial M_r} + \frac{\chi_F}{\rho c} F , \tag{A10}$$

$$\frac{D}{Dt}\left(e + \frac{E}{\rho}\right) + \left[f \frac{D}{Dt}\left(\frac{1}{\rho}\right) - (3f - 1)\frac{v}{\rho r} \right] E + (p + Q)\frac{D}{Dt}\left(\frac{1}{\rho}\right) = \epsilon_{\rm CR} - \frac{\partial (4\pi r^2 F)}{\partial M_r} , \tag{A11}$$

$$\frac{1}{c^2}\frac{DF}{Dt} + \frac{4\pi r^2 \rho}{q}\frac{\partial (fqE)}{\partial M_r} = -\frac{\chi_F F}{c} , \tag{A12}$$

$$\frac{D}{Dt}\left(\frac{E}{\rho}\right) + \left[f \frac{D}{Dt}\left(\frac{1}{\rho}\right) - (3f - 1)\frac{v}{\rho r} \right] E = \frac{1}{\rho}(4\pi \chi_P B - c\chi_E E) - \frac{\partial (4\pi r^2 F)}{\partial M_r} , \tag{A13}$$

where Q is the artificial viscosity in the formulation of von Neumann & Richtmeyer (1950), and the sphericality factor q is defined by (Auer 1971)

$$\ln q = \int_{R_{\rm in}}^{r} \frac{3f - 1}{fr'}\, dr' .$$

These equations are closed when the *scalar* Eddington factor and the equation of state (5) are given. The internal energy density e and the gas pressure p are replaced by T and ρ using the equation of state, which is mentioned in § 4.4.

The six variables r, ρ, v, T, E, and F are solved as functions of mass. For spatial differencing of the equations, ρ, T, and E are defined at the center of each grid cell, and r, v, and F are on the interfaces that bound the cell. We thus obtain vectors of the variables $(r_i, \rho_{i+1/2}, v_i, T_{i+1/2}, E_{i+1/2}, F_i)$, which are to be solved in a fully implicit scheme. The system is linearized around the trial estimates $(r_i^*, \rho_{i+1/2}^*, v_i^*, T_{i+1/2}^*, E_{i+1/2}^*, F_i^*)$ to obtain an $(I \times I)$ block tridiagonal system of (6×6) matrices, where I is the number of grid cells. The solution vectors $(\delta r_i, \delta\rho_{i+1/2}, \delta v_i, \delta T_{i+1/2}, \delta E_{i+1/2}, \delta F_i)$ are solved by Gaussian elimination.

In contrast to implicit method, explicit methods are constrained by the CFL condition, which assures numerical stability (Courant, Friedrichs, & Levy 1928),

$$(|v| + c)\Delta t \le \Delta r , \tag{A14}$$

where v, c, Δt, and Δr are the fluid velocity, the speed of transport of information, the time step, and the width of the grid, respectively. Solving the moment equations of radiation on an explicit scheme would require an unacceptably small value of Δt compared to the evolutionary timescale because c in (A14) is the speed of light in this case. Then, the moment equations of radiation (A12) and (A13) with the fluid energy equation (A11) are often solved on an implicit scheme while the fluid motion can be solved explicitly for some cases. However, the CFL condition that rules the equation of motion (A10)—i.e., equation (A14) in which c is now replaced by the speed of sound—still imposes such a severe restriction that explicit methods are ruled out in numerical calculations for the whole evolution of protostellar collapse (Tscharnuter & Winkler 1979). It is therefore imperative that the full set of equations (A8)–(A13) is solved with an implicit scheme.

The frequency-averaged absorption coefficients χ_E, χ_F, and χ_P and Eddington factor f_E are needed in order to solve equations (A8)–(A13). The weighting values E_ν and F_ν, or J_ν and H_ν, are given by direct integration of I_ν over μ. We explain the method for calculating J_ν and H_ν afterward. The frequency-averaged values are obtained using the solved spectral profiles J_ν and H_ν as

$$\chi_F = \frac{\int_0^\infty \chi_\nu H_\nu\, d\nu}{H} , \tag{A15}$$

$$\chi_E = \frac{\int_0^\infty \chi_\nu J_\nu \, d\nu}{J} , \tag{A16}$$

$$\chi_P = \frac{\int_0^\infty \chi_\nu B_\nu \, d\nu}{\sigma T^4/\pi} , \tag{A17}$$

and

$$f_E = \frac{\int_0^\infty f_\nu J_\nu \, d\nu}{J} , \tag{A18}$$

where

$$J = \int_0^\infty J_\nu \, d\nu ,$$

$$H = \int_0^\infty H_\nu \, d\nu .$$

The entire procedure at each time step is carried out as follows.

1. Trial estimates of density and temperature structures [$\rho(r)$ and $T(r)$] are assumed.
2. Equations (A1) and (A2) are solved under the given density and temperature distributions to calculate the first three moments for radiation equations (A5), (A6), and (A7).
3. The integrations over frequency equations (A15)–(A18) are carried out to obtain $f_E(r)$, $\kappa_E(r)$, $\kappa_F(r)$, and $\kappa_P(r)$.
4. Equations (A8)–(A13) are solved using the given Eddington factor and mean opacities and then yield improved density and temperature distributions, with which the transfer equation is solved again.
5. We iterate steps (1)–(4) until it converges sufficiently.

One thus obtains the radiation hydrodynamic quantities that are consistent with the radiation field at each time step. Trial estimates of an iterative procedure are given by the solutions at the previous time step.

A3. THE ENERGY MEAN AND FLUX MEAN OF OPACITY

In the transfer equation solver, the mean opacities (κ_E, κ_F, and κ_P) are calculated, as well as the Eddington factor. We note here how to obtain $J_\nu(r)$ and $H_\nu(r)$, which are required for calculating the mean opacities in equations (A16)–(A17).

MM suggested that $J_\nu(r)$ and $H_\nu(r)$ should be obtained by solving the monochromatic moment equations of radiation using the current estimates of $T(r)$ and $f_\nu(r)$ (MM p. 484). However, one can obtain $J_\nu(r)$ and $H_\nu(r)$ directly also by integrating $I_\nu(r, \mu)$ and $\mu I_\nu(r, \mu)$ over μ. The former method, however, has a serious problem for nongray calculations as described below.

In a nongray calculation the Planck function, B_ν, increases exponentially with temperature at a frequency in the Wien regime, in contrast to the gray approximation, for which B is only proportional to T^4. Therefore, even a moderate contrast of temperature throughout a computational region sometimes requires an extremely wide dynamic range for I_ν. For instance, an evolved protostar has a central core of $T \gtrsim 3000$ K with a cold envelope of $T \sim 10$ K. Such a situation involves a great range of I_ν over 100 orders of magnitude at $\nu \sim 10^{14}$ Hz throughout the computational region. It exceeds the available numerical range by far for ordinary computational tools. Thus, J_ν, H_ν, and K_ν in the cold region at high frequency should equal zero numerically. In such cases the Eddington factor is not easily obtained because $f_\nu \equiv J_\nu/K_\nu$ is not well-defined numerically, although the actual Eddington factor should behave regularly however close the individual values of J_ν and K_ν are to zero. If the Eddington factor is not obtained, one cannot solve the moment equations.

In contrast to the method suggested by MM, we calculate the moments of radiation directly by integrating $I_\nu(r, \mu)$ over μ instead of solving the monochromatic moment equations in the transfer equation solver. Our method works well even in the case where J_ν and K_ν are very small.

A4. COORDINATES FOR COMPUTATION

Calculations are performed on the Lagrangian coordinates for the initial isothermal collapse, and the Eulerian takes the place after the adiabatic core is formed, i.e., after the accretion shock is generated. This method was found to successfully resolve the accretion shock at the surface of the first core in our calculations. For Eulerian calculations we introduce second-order accurate advection, supplementing the Lagrangian RHD equations (A8)–(A13).

For discretization we use 200 radial grid cells and 20 frequency bins. The paths along which the transfer equation is integrated are set tangentially to each radial grid (see Fig. 13). The innermost zone has 30 additional paths, so as to provide a sufficient number of angle-mesh points for innermost rings of the radial grid. The initial radial grid is set up as $\Delta \log r = \text{constant}$.

APPENDIX B

TEST CALCULATIONS FOR RADIATION

To check the abilities of the moment equations solver, the transfer equation solver, and the convergence between them, test calculations for the numerical code are presented briefly in this section. Because the moment equations of radiation are

difficult to solve analytically when they are coupled with hydrodynamics, effects of radiation are investigated separately from hydrodynamics here (see Ensman 1994). Test calculations for hydrodynamics are not presented in this paper, but we have checked that numerical results of some hydrodynamic tests show good agreements with analytical predictions.

For radiation tests, material is assumed to be static, with the right-hand side of equation (A10) set to zero. For simplicity, the density distribution is assumed to be homogeneous and radiation to be gray. Then, suppose small fluctuations of temperature in radiative equilibrium. The fluctuation should be smoothed out by radiation quasi-statically if the radiation energy density is sufficiently small compared to the internal energy density of material. This mode is called the "thermal relaxation mode" of radiation (MM p. 510). The relaxation rate $n(k)$ for a perturbation with wavenumber k is (Spiegel 1957)

$$n(k) = v\left[1 - \frac{\chi_0}{k}\cot^{-1}\frac{\chi_0}{k}\right], \tag{B1}$$

where

$$v = \frac{16\sigma\chi_0 T_0^3}{\rho c_v}, \tag{B2}$$

where c_v is the heat capacity of material and subscript zero represents unperturbed quantities.

Spiegel (1957) derived equation (B1) for a perturbation of plane wave, i.e., $e^{i\mathbf{k}\cdot\mathbf{x}}$. However a *spherical* wave solution is required for the test of our numerical scheme. We have found that the zeroth-order spherical Bessel function, $j_0(r) \equiv \sin kr/kr$, is the eigenfunction in the spherical case, and it yields the exactly same dispersion relation as equation (B1). See Appendix C for derivation.

Figure 14 shows relaxation of a fluctuation of the spherical wave $j_0(kr)$ in the case of the total optical depth of 10. The unperturbed temperature distribution is homogeneous at 10 K. A temperature disturbance (Fig. 14*a*) damps toward the unperturbed state. The radiation temperature $T_{\rm rad} \equiv (E_{\rm rad}/a)^{1/4}$ (Fig. 14*b*) damps correspondingly to the relaxation of the material temperature, but slightly more rapidly. For more opaque material, of course, the difference between T and $T_{\rm rad}$ would be smaller.

The dispersion relations are shown in Figure 15. The ordinate represents $n(k)t_\lambda$, where $t_\lambda \equiv (c\chi)^{-1}$ is the mean flight time of a photon. The ordinate therefore means how much a temperature disturbance decays while a photon travels over a mean free path. First, to test the moment equations solver solely, we calculate the thermal relaxation mode in the Eddington approximation, fixing $f_E \equiv \frac{1}{3}$ instead of solving the transfer equation solver. In this case equation (B1) reduces to the dispersion relation under the Eddington approximation (Unno & Spiegel 1966),

$$n_E(k) = \frac{v}{1 + 3(\chi_0/k)^2}. \tag{B3}$$

The numerical results show good agreement with equation (B3) in Figure 15*a*. Therefore the moment equations are found to be solved correctly.

Second, accuracy in the transfer equation solver is tested. In Figure 15*b*, the numerical result that was obtained using the Eddington factors calculated by the transfer equation solver is plotted with the analytical dispersion relation (eq. [B1]). They agree, again, with each other within a relative error of one percent. These results guarantee the accuracy of the method over a wide range in optical depth.

APPENDIX C

THERMAL RELAXATION MODE IN SPHERICAL SYMMETRY

The thermal relaxation mode of a radiating fluid was investigated first by Spiegel (1957). He derived the dispersion relation (B1) for a perturbation of a plane wave, which inevitably requires that the temperature distribution must be in slab symmetry. We will show that a temperature disturbance in spherical symmetry decays in the same rate as given by equation (B1).

We assume that there are no fluid motions and no heat sources, and the radiation field is gray. The fluid energy equation (3), then, reduces to

$$\rho\frac{\partial e}{\partial t} = 4\pi\chi(J - B), \tag{C1}$$

where $J \equiv (1/4\pi)\oint I\, d\Omega = (c/4\pi)E$ is the mean intensity and χ is a gray opacity per unit volume. The source function in LTE, B, can be replaced by $(\sigma/\pi)T^4$.

The specific intensity I is determined by the transfer equation,

$$\frac{\partial I}{\partial s} = -\chi(I - B), \tag{C2}$$

where we have neglected the transit time of radiation.

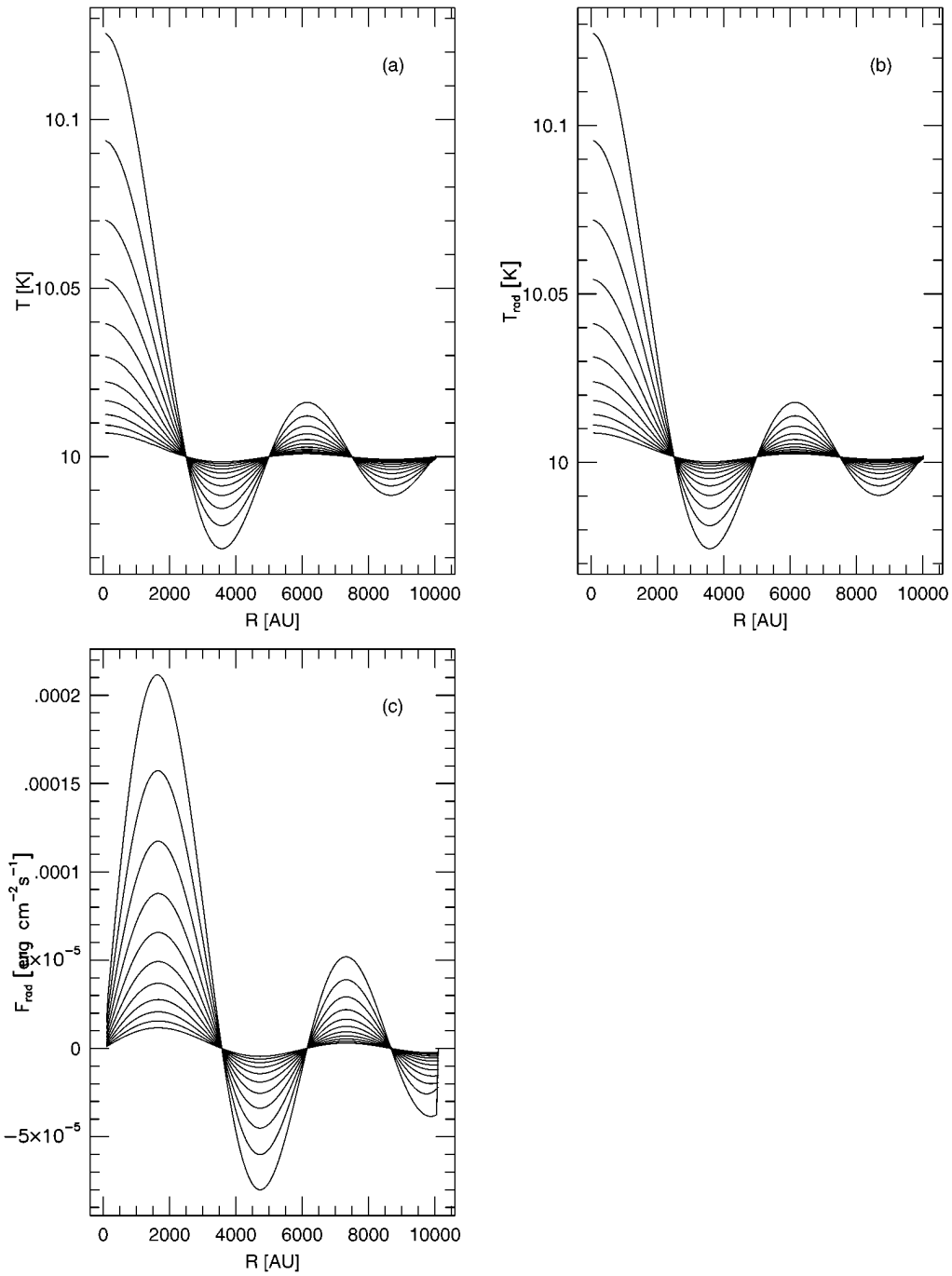

FIG. 14.—Results of test calculations for the thermal relaxation mode. (*a*) Relaxation of a small disturbance of temperature. The given perturbation (the curve of the largest amplitude) decays to a homogeneous distribution. (*b*) Relaxation of radiation temperature. (*c*) Relaxation of radiative flux.

For linearizing the above two equations, we write the temperature as follows, neglecting the terms of higher order fluctuation.

$$T(r, t) = T_0(r) + T_1(r, t) . \tag{C3}$$

The other quantities are written as

$$B(r, t) = B_0(r) + \frac{\partial B_0}{\partial T} T_1 \equiv B_0 + B_1 , \tag{C4}$$

$$\chi(r, t) = \chi_0(r) + \frac{\partial \chi_0}{\partial T} T_1 \equiv \chi_0 + \chi_1. \tag{C5}$$

Using equations (C3), (C4), and (C5), equations (C1) and (C2) are reduced to the following equation, which describes the relaxation of the temperature disturbance (MM p. 509).

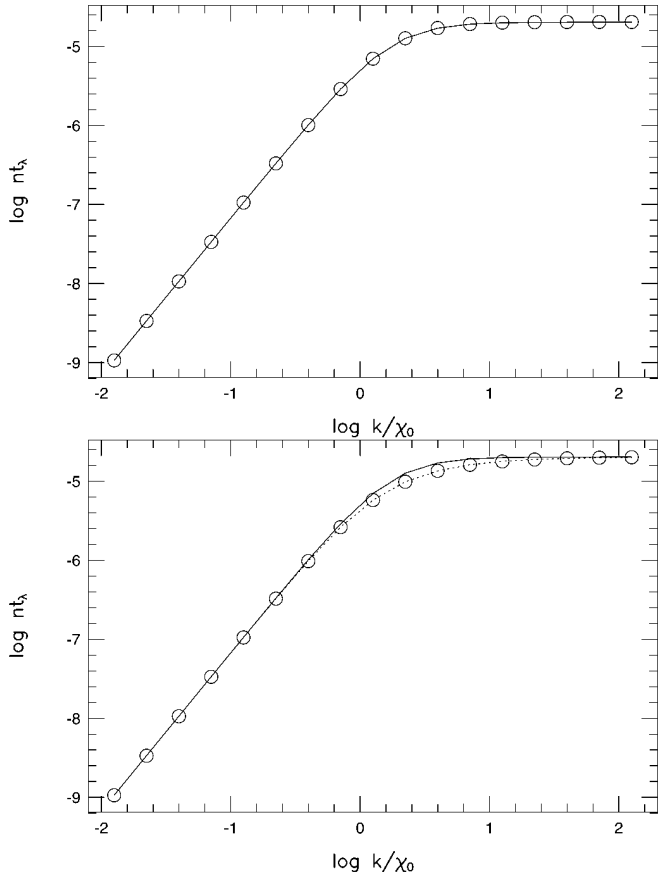

FIG. 15.—Dispersion relation for the thermal relaxation mode of radiation. See text for the physical meanings of the axes. *Top:* The dispersion relation under the Eddington approximation. Solid line is the analytical solution, and open circles denote the numerical results with $f \equiv \frac{1}{3}$. *Bottom:* The exact dispersion relation without the Eddington approximation. Dotted line corresponds to the exact solution, and open circles denote the numerical results obtained by using the variable Eddington factor.

$$\frac{\partial T_1(\boldsymbol{r})}{\partial t} = -v\left[T_1(\boldsymbol{r}) - \frac{1}{4\pi} \oint d\Omega \int_0^\infty \chi_0 \, ds \, T_1(\boldsymbol{r} - \boldsymbol{n}s) e^{-\chi_0 s} \right], \tag{C6}$$

where $\boldsymbol{n}$ is the unit direction vector along a light ray and v is defined in equation (B2).

The terms including χ_1 have vanished because of the assumptions that the unperturbed radiation field is isotropic and in radiative equilibrium. All the assumptions introduced above are the same as those by Spiegel (1957).

Equation (C6) admits separable solutions of the following form for spherical symmetric cases,

$$T_1(r, t) = \phi(k, t) j_0(kr) , \tag{C7}$$

where $j_0(x) \equiv \sin x/x$ is the 0th order spherical Bessel function.

Substituting equations (C7) and $r' \equiv \boldsymbol{r} - \boldsymbol{n}s$ into (C6) rewritten in the cylindrical coordinates (r, μ), where μ is the direction cosine,

$$\frac{\partial \phi}{\partial t} = -v \left[1 - \frac{1}{2} \int_{-1}^{1} d\mu \int_0^\infty d\tau \, e^{-\tau} \frac{j_0(kr')}{j_0(kr)} \right] \phi , \tag{C8}$$

where $\tau \equiv \chi_0 s$.

For the purpose of replacing r' with τ and μ, let the path of a light ray s be written down explicitly (see Fig. 16),

$$s = \pm [r'^2 - r^2(1 - \mu^2)]^{1/2} + r\mu . \tag{C9}$$

The negative sign in the first term in right-hand side is required only for $r' < r$. After rearranging equation (C9) and replacing s with τ, we have

$$\xi \equiv kr' = \frac{k}{\chi_0} [\tau^2 - 2\tau\chi_0 r\mu + (\chi_0 r)^2]^{1/2} , \tag{C10}$$

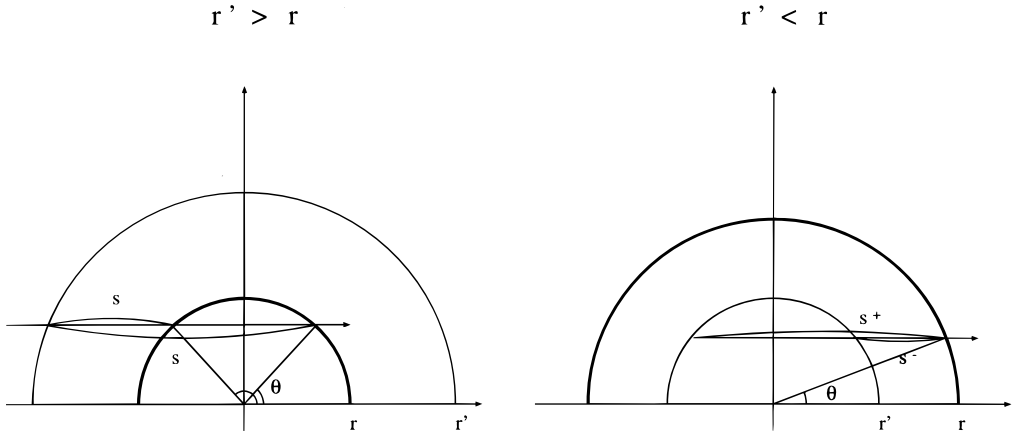

FIG. 16.—Illustration of the path of integration, s. See Appendix C.

and

$$d\mu = -\frac{\chi_0 \xi}{\tau r k^2}\, d\xi \,,$$

$$\xi_{-1} \equiv \xi(\mu = -1) = \frac{k}{\chi_0}(\tau + \chi_0 r),\ \xi_1 \equiv \xi(\mu = 1) = \frac{k}{\chi_0}|\tau - \chi_0 r| \,.$$

After integrating over ξ instead of μ, the last term in equation (C8) equals

$$\frac{\chi_0}{2rk^2}\int_0^\infty d\tau\, \frac{e^{-\tau}}{\tau}\, \frac{\cos\,\xi_1 - \cos\,\xi_{-1}}{j_0(kr)} = \frac{\chi_0}{k}\int_0^\infty d\tau\, e^{-\tau}\, \frac{\sin\,(k/\chi_0\tau)}{\tau} \,.$$

The last integral is reduced to $\cot^{-1}\chi_0/k)$. Hence, equation (C8) becomes

$$\frac{\partial \phi}{\partial t} = -\nu\left[1 - \frac{\chi_0}{k}\cot^{-1}\left(\frac{\chi_0}{k}\right)\right]\phi \,. \tag{C11}$$

The thermal relaxation rate $n(k)$ is defined as

$$\frac{\partial \phi}{\partial t} = -n(k)\phi \,. \tag{C12}$$

Comparing equations (C11) and (C12), we have equation (B1).

REFERENCES

Adams, F. C., & Shu, F. H. 1986, ApJ, 308, 836
André, P., Ward-Thompson, D., & Barsony, M. 1993, ApJ, 406, 122
Appenzeller, I., & Tscharnuter, W. 1974, A&A, 30, 423
Auer, L. H. 1971, J. Quant. Spectrosc. Radiat. Transfer, 11, 573
Black, D. C., & Bodenheimer, P. 1975, ApJ, 199, 619
Bodenheimer, P., & Sweigart, A. 1968, ApJ, 152, 515
Boss, A. P. 1984, ApJ, 277, 768
———. 1988, ApJ, 331, 370
Boss, A. P., & Myhill, E. A. 1992, ApJS, 83, 311
Boss, A. P., & Yorke, H. W. 1995, ApJ, 439, L55
Buchler, J. R. 1979, J. Quant. Spectrosc. Radiat. Transfer, 22, 293
Castor, J. I. 1972, ApJ, 178, 779
Chandrasekhar, S. 1967, An Introduction to the Study of Stellar Structure (New York: Dover)
Chick, K. M., Pollack, J. B., & Cassen, P. 1996, ApJ, 461, 956
Courant, R., Friedrichs, K. O., & Levy, H. 1928, Math. Ann., 100, 32
Efstathiou, A., & Rowan-Robinson, M. 1990, MNRAS, 245, 275
———. 1991, MNRAS, 252, 528
Ensman, L. 1994, ApJ, 424, 275
Goldsmith, P. F., & Langer, W. D. 1978, ApJ, 222, 881
Inutsuka, S., & Miyama, S. M. 1997, ApJ, 480, 681
Kenyon, S. J., Calvet, N., & Hartmann, L. 1993, ApJ, 414, 676
Lada, C. J. 1987, in IAU Symp. 115, Star Forming Regions, ed. M. Peimbert & J. Jugaku (Dordrecht: Reidel), 1
Larson, R. B. 1969, MNRAS, 145, 271
Mihalas, D., & Mihalas, B. W. 1984, Foundations of Radiation Hydrodynamics (New York: Oxford Univ. Press) (MM)
Mizuno, A., Onishi, T., Hayashi, M., Ohashi, N., Sunada, K., Hasegawa, T., & Fukui, Y. 1994, Nature, 368, 719
Narita, S., Nakano, T., & Hayashi, C. 1970, Prog. Theor. Phys., 43, 942
Penston, M. V. 1969, MNRAS, 144, 425
Pollack, J. B., Hollenbach, D., Beckwith, S., Simonelli, D. P., Roush, T., & Fong, W. 1994, ApJ, 421, 615
Preibisch, T., Sonnhalter, C., & Yorke, H. W. 1995, A&A, 299, 144
Shu, F. H. 1977, ApJ, 214, 488
———. 1995, in Molecular Clouds and Star Formation, ed. C. Yuan & J. H. You (Singapore: World Scientific), 97
Shu, F. H., Adams, F. C., & Lizano, S. 1987, ARA&A, 25, 23
Spiegel, E. A. 1957, ApJ, 126, 202
Stahler, S. W., Shu, F. H., & Taam, R. E. 1980, ApJ, 241, 637
Stone, J. M., Mihalas, D., & Norman, M. L. 1992, ApJS, 80, 819 (SMN)
Tscharnuter, W. M., & Winkler, K.-H. 1979, Comp. Phys. Comm., 18, 171
Unno, W., & Spiegel, E. A. 1966, PASJ, 18, 85
von Neumann, J., & Richtmeyer, R. D. 1950, J. Appl. Phys., 21, 232
Ward-Thompson, D., Scott, P. F., Hills, R. E., & André, P. 1994, MNRAS, 268, 276
Winkler, K.-H. A., & Newman, M. J. 1980a, ApJ, 236, 201 (WNa)
———. 1980b, ApJ, 238, 311 (WNb)
Yorke, H. W. 1979, A&A, 80, 308
———. 1980, A&A, 85, 215
Yorke, H. W., Bodenheimer, P., & Laughlin, G. 1993, ApJ, 411, 274
———. 1995, ApJ, 443, 199